# Spin-flip Raman scattering in $n$-type diluted magnetic semiconductors

D. L. Peterson, D. U. Bartholomew, U. Debska, A. K. Ramdas, and S. Rodriguez
*Department of Physics, Purdue University, West Lafayette, Indiana 47907*
(Received 14 January 1985)

We report the results of a spin-flip Raman scattering study of electrons bound to shallow donors in the diluted magnetic semiconductors $Cd_{1-x}Mn_xTe$ and $Cd_{1-x}Mn_xSe$ for $x \lesssim 0.30$ and in $Cd_{1-x}Mn_xS$ for $x=0.022$ and 0.125. Spin-flip Raman scattering is observed at temperatures ranging from 1.8 K to as high as 160 K and at magnetic fields $\leq 60$ kG. The measured spin-flip energies are large and, for some samples, correspond to $g$ values in excess of 100 at low temperatures. The enhancement of the Raman shifts results from the exchange coupling of the donor electron with the $Mn^{2+}$ ions. The parameters of the mean-field approximation, used to describe the magnetic field and temperature dependence of $g$ are shown to exhibit a temperature dependence for temperatures above 20 K. Finite Raman shifts are observed in the absence of a magnetic field and are attributed to the bound magnetic polaron and thermal fluctuations of the local magnetization. The temperature and magnetic field dependences of the spin-flip energies, Raman intensities, and polarizations were compared with the results of the statistical-mechanical model of Dietl and Spałek [Phys. Rev. B **28**, 1548 (1983)]. The theory is in good agreement with the experimental results for $x \lesssim 0.15$.

## I. INTRODUCTION

Since the first observations of electron spin-flip Raman scattering in the narrow-band-gap semiconductor InSb by Slusher, Patel, and Fleury,[1] followed by that in the wide-band-gap semiconductor CdS by Thomas and Hopfield,[2] there has been a continuing interest in this magneto-optical phenomenon. An important contribution to this field is the first demonstration of the spin-flip Raman laser by Patel and Shaw.[3] The success of the InSb spin-flip Raman laser as a practical source of magnetic-field-tuned, coherent radiation in the (5–15) $\mu$m spectral region[3,4] can be traced to the large effective $g$ factor of the electron, $|g^*| \simeq 50$. In contrast, the wider-band-gap II-VI compound semiconductors CdS, CdSe, and CdTe have rather small spin splittings[2,5] characterized by $|g^*| \lesssim 2$, since their conduction- and valence-band spin-orbit interactions are small in comparison to their energy-band gaps.

The substitution of the magnetic ion $Mn^{2+}$ for the cation in a II-VI compound semiconductor results in a class of alloys—the diluted magnetic semiconductors (DMS's)—which exhibits novel semiconducting and magnetic properties.[6] The strong exchange coupling between the $3d$ electrons of $Mn^{2+}$ and the band electrons[7] underlies a variety of magneto-optical phenomena observed in DMS's. For example, the free exciton in $Cd_{1-x}Mn_xTe$, the prototype for wide-band-gap DMS's, undergoes a large splitting[8] in a moderate magnetic field and results in the observed giant Faraday rotation;[9] these effects can be characterized by an effective $g$ factor for the band electrons, 2 orders of magnitude larger than that for CdTe.

When detectable, spin-flip Raman scattering provides a practical means of probing the electronic structure of semiconductors, as dramatically illustrated in DMS's. The large Raman shifts associated with spin-flip scattering from electrons in DMS's were first observed in the narrow-band-gap $Hg_{1-x}Mn_xTe$ by Geyer and Fan.[10] The first evidence of a finite spin splitting of the electronic level in the absence of a magnetic field was reported by Nawrocki *et al.*[11] in the wide-band-gap diluted magnetic semiconductor $Cd_{1-x}Mn_xSe$. The effects of Mn concentration and the antiferromagnetic coupling among the $Mn^{2+}$ ions on the spin-flip Raman shifts were first observed[12] in a study of $Cd_{1-x}Mn_xTe$. These studies established the nature of Raman scattering associated with the spin-flip transitions of electrons bound to donors in DMS's. The large Raman shifts depend not only on the applied magnetic field, but also on temperature and manganese concentration. The far-infrared absorption spectra[13] of $Cd_{1-x}Mn_xSe$ also provided evidence of these spin-flip transitions. Following these initial reports, there have been several investigations[14–19] of spin-flip Raman scattering in DMS's for isolated compositions or over limited temperature ranges. The results presented in this paper represent a detailed study of spin-flip Raman scattering in intentionally doped $Cd_{1-x}Mn_xTe$ for compositions in the range $0.01 \leq x \leq 0.30$. These alloys were investigated for magnetic fields up to 60 kG and temperatures ranging from 1.8 to 40 K. The corresponding study of $Cd_{1-x}Mn_xSe$ for compositions $0.01 \leq x \leq 0.30$ and temperatures $1.8\ \text{K} \leq T \leq 160$ K yields a much more complete set of results than previously reported. In addition, two compositions of $Cd_{1-x}Mn_xS$, $x=0.02$ and 0.10, were studied as illustrative examples, allowing a comparison of these three systems of alloys. The extensive results obtained in the present study allow a detailed comparison with the theory of Dietl and Spałek.[20,21]

## II. EXPERIMENT

### A. Sample growth and preparation

$Cd_{1-x}Mn_xTe$ crystals can be grown for Mn concentrations of $x \leq 0.75$ and have the cubic zinc-blende struc-

 

ture.[22] $Cd_{1-x}Mn_xSe$ and $Cd_{1-x}Mn_xS$ have the hexagonal wurtzite structure, and can be grown with $x \leq 0.50$ and $x \leq 0.45$, respectively.[22] The crystals used in our investigation were grown by the Bridgman method with the nominal $x$ values given in Table I. These values agree for the most part with the actual concentrations which were determined by electron-probe microanalysis. The most significant discrepancies between the nominal and measured values of $x$ occurred for the $Cd_{1-x}Mn_xTe$:Ga, $x=0.20$, $Cd_{1-x}Mn_xSe$:In, $x=0.20$, and $Cd_{1-x}Mn_xS$, $x=0.10$, samples. In this paper, for convenience, the samples will usually be referred to by their nominal values of $x$. The energy gaps of diluted magnetic semiconductors vary with $x$. For $Cd_{1-x}Mn_xTe$, $E_g = 1.595 + 1.592x$ eV at liquid-helium temperatures,[23] while the energy gap for the $A$ exciton in $Cd_{1-x}Mn_xSe$ follows[24] $E_g^A = 1.82 + 1.50x$ eV.

The magnetic phase transitions of $Cd_{1-x}Mn_xTe$, $Cd_{1-x}Mn_xSe$, and $Cd_{1-x}Mn_xS$ have been studied in detail.[25–27] All three alloy types are paramagnetic for high temperatures and exhibit a paramagnetic to spin-glass phase transition at lower temperatures. The presence of the spin-glass phase is a consequence of frustration in an fcc or hcp lattice when the magnetic ions interact antiferromagnetically.[28] The onset of lattice frustration occurs at a "percolation" concentration which depends on the topology of the lattice, not on the specific ions involved. Since the zinc-blende and wurtzite crystal structures are essentially identical up to nearest neighbors, the percolation concentration ($x \sim 0.17$–$0.19$) is the same for the three diluted magnetic systems considered here. In addition to the paramagnetic to spin-glass phase transition, $Cd_{1-x}Mn_xTe$ exhibits a paramagnetic to antiferromagnetic phase transition for $x \gtrsim 0.60$.

For electron spin-flip Raman scattering studies to be successful it is necessary to have a sufficient number of neutral donors at low temperatures. Due to cation vacancies, which behave as doubly charged acceptors,[29] most $Cd_{1-x}Mn_xTe$ crystals exhibit $p$-type conductivity. We note, however, that even without intentional doping, a sufficient number of donors may be accidentally introduced.[12] In order to guarantee a sufficient number of neutral donors for Raman scattering, it is necessary to intentionally dope the crystals by introducing impurities into the melt. Preliminary attempts at doping $Cd_{0.97}Mn_{0.03}Te$ with In (substituting for Cd) and $Cd_{0.94}Mn_{0.06}Te$ with Cl (substituting for Te) were unsuccessful. Intentional doping of $Cd_{1-x}Mn_xTe$ was achieved by using Ga as the impurity substituting for the cation. This method produced a sufficient number of neutral donors in $Cd_{1-x}Mn_xTe$ for $x \leq 0.10$. Presumably due to an increasing number of vacancies in the Cd-Mn sublattice, this method was not successful for higher manganese concentrations. Several attempts were made to decrease the number of cation vacancies by annealing; for example, keeping $Cd_{1-x}Mn_xTe$:Ga, $x=0.30$, in Cd vapor at 900 °C for five days produced enough neutral donors to allow the observation of spin-flip Raman signal. Attempts at producing $n$-type $Cd_{0.40}Mn_{0.60}Te$ have to date been unsuccessful. In contrast to the difficulties encountered in producing $n$-type $Cd_{1-x}Mn_xTe$, "as-grown" $Cd_{1-x}Mn_xSe$ crystals are $n$ type, similar to the well-known behavior of CdSe. However, as $x$ is increased, it becomes necessary to intentionally introduce additional donors into $Cd_{1-x}Mn_xSe$ to increase the Raman signal. This may also be due to an increasing number of Cd-Mn vacancies. Adding In to the melt for $Cd_{1-x}Mn_xSe$, $x=0.20$ and 0.30, increased the density of neutral donors to a level sufficient for Raman scattering. This method did not work for the highest concentrations, such as $x=0.45$.

The samples were oriented using the Laue method and optically polished according to the following procedure. The surfaces were ground in succession with 600-, 1200-, and 3200-grit carborundum powder. The initial polish was done on nylon cloth using 6-$\mu$m diamond paste. The final polish was done on microcloth saturated with a suspension of 0.05-$\mu$m alumina powder in distilled water. This process produced samples whose polished surfaces are within 2° of the desired orientation.

### B. Experimental procedure

The Raman spectra were excited using the 7993-, 7525-, 6764-, 6471-, 5682-, or 5309-Å line of a $Kr^+$-ion laser or the 5145- or 5017-Å line of an $Ar^+$-ion laser. Since the Raman feature studied in this investigation exhibits a strong temperature dependence, it was necessary to adjust the power of the exciting laser to prevent heating of the samples due to absorption. This was accomplished by lowering the power until the Raman shift was no longer affected. This usually resulted in using laser powers on the order of 2–5 mW. For the $Cd_{1-x}Mn_xTe$:Ga, $x=0.30$, sample, it was necessary to use a laser power of 50 mW in order to observe the spin-flip signal; this may have resulted in some heating of this sample. The gallium-doped $Cd_{1-x}Mn_xTe$ samples exhibited an absorption edge $\sim 1000$ $cm^{-1}$ below the expected energy-band gap. This additional absorption decreased with annealing and may be attributed to defect levels associated with vacancy-donor complexes.[29] The laser wavelengths used to excite the Raman spectra in each sample are listed in Table I. The scattered light was analyzed using a computer-controlled double (triple) monochromator and detected using a standard photon-counting system.[30] As needed, the triple monochromator was used to reduce stray light, enabling us to observe weak Raman features to within 3 $cm^{-1}$ of the exciting laser line.

The samples were inserted in a variable-temperature optical magnetic cryostat[30] equipped with a superconducting coil, which enabled us to apply external magnetic fields up to 60 kG. The sample temperature was measured using a calibrated carbon-glass resistor located on the copper sample holder, immediately above the sample. A temperature controller provided a stabilized temperature over the range 1.8–300 K.

As discussed in a subsequent section, the intensity of the spin-flip Raman line decreases as the Raman shift decreases. As a result, the difficulty of observing Raman features within 5 $cm^{-1}$ of the laser line due to the presence of parasitic radiation is further aggravated. This made the observation of the spin-flip signal for small magnetic fields very difficult in some samples, particularly the $Cd_{1-x}Mn_xTe$ samples. The peak Raman intensity

TABLE I. Sample characteristics and experimental parameters.

| DMS system | Impurity | Sample | Mn concentration ($x$) Nominal | Mn concentration ($x$) Measured | Laser wavelength (Å) | Temperature range (K) |
|---|---|---|---|---|---|---|
| $Cd_{1-x}Mn_xTe$ | | GA1 | 0.01 | | 7993 | 1.8—20 |
| | Ga | P75 | 0.03 | 0.035 | 7993 | 1.8—40 |
| | Ga | GI613 | 0.05 | 0.044 | 7993 | 1.8—40 |
| | Ga | P30 | 0.10 | 0.102 | 7525 | 1.8—40 |
| | Ga | P84A | 0.20 | 0.250 | 6764 | 1.8—20 |
| | Ga | P38C | 0.30 | 0.295 | 6764 | 1.8—20 |
| $Cd_{1-x}Mn_xSe$ | | GI553 | 0.01 | 0.012 | 7525 | 1.8—40 |
| | | GI552 | 0.05 | 0.051 | 7525 | 1.8—40 |
| | | GI551 | 0.10 | 0.104 | 7525, 6764 | 1.8—160 |
| | In | P48 | 0.20 | 0.129 | 6764, 6471 | 1.8—80 |
| | In | P66 | 0.30 | 0.311 | 5682 | 1.8—40 |
| $Cd_{1-x}Mn_xS$ | | EP3 | 0.02 | 0.022 | 5145, 5017 | 1.8—40 |
| | | EP13 | 0.10 | 0.125 | 5309 | 1.8—40 |

also decreases with increasing temperature. This effect prevented the observation of spin-flip Raman scattering in some samples for $T>20$ K. A strong photoluminescence background allowed the observation of spin-flip Raman scattering in $Cd_{1-x}Mn_xTe$:Ga, $x=0.20$, and $Cd_{1-x}Mn_xSe$:In, $x=0.30$, only over a limited range of magnetic fields. The temperature ranges for which spin-flip Raman scattering was observed in each sample are given in Table I.

The light-scattering experiments were performed using the right-angle scattering geometry. In this geometry, the external field $\mathbf{H}$ was applied along the direction of either the incident ($\hat{\mathbf{k}}_i$) or the scattered ($\hat{\mathbf{k}}_s$) beam. With $\mathbf{H}||\hat{\mathbf{k}}_i||\hat{\mathbf{z}}$, the incident beam passes through a Babinet-Soleil compensator, set to produce circularly polarized light of either positive ($\hat{\boldsymbol{\sigma}}_+$) or negative ($\hat{\boldsymbol{\sigma}}_-$) helicities, where $\hat{\boldsymbol{\sigma}}_\pm=(\hat{\mathbf{x}}\pm i\hat{\mathbf{y}})/\sqrt{2}$, and the scattered light is analyzed along the direction of the magnetic field ($\hat{\mathbf{z}}$). This light-scattering configuration will be referred to as ($\hat{\boldsymbol{\sigma}}_\pm,\hat{\mathbf{z}}$). In the right-angle geometry with $\mathbf{H}||\hat{\mathbf{k}}_s$, the incident light is polarized along the direction of the magnetic field ($\hat{\mathbf{z}}$), and the polarization of the scattered radiation is analyzed as either $\hat{\boldsymbol{\sigma}}_+$ or $\hat{\boldsymbol{\sigma}}_-$ using a quarter-wave plate in combination with a linear analyzer. For the $Cd_{1-x}Mn_xSe$ and $Cd_{1-x}Mn_xS$ samples, the uniaxial direction was kept parallel to the magnetic field ($\hat{\mathbf{c}}||\mathbf{H}$) to within 5°.

## III. EXPERIMENTAL RESULTS AND DISCUSSION

### A. Characteristics of spin-flip Raman scattering in DMS's

In order to describe the variety of magnetic excitations observed in Raman scattering, it is useful to consider the Hamiltonian of the $Mn^{2+}$ spins $\{\mathbf{S}_i\}$ and that of one electron, $\mathbf{s}$, in the presence of an applied magnetic field. We consider the electron to be either in the conduction band or bound to a donor in an extended, effective-mass state. Representing the exchange interactions by the Heisenberg form, the Hamiltonian of this system can be written as

$$H_M(\{\mathbf{S}_i\},\mathbf{s})=-\alpha N_0\sum_i \mathbf{S}_i\cdot\mathbf{s}+g^*\mu_B\mathbf{H}\cdot\mathbf{s} +g\mu_B\mathbf{H}\cdot\sum_i\mathbf{S}_i+\sum_{i<j}J_{ij}\mathbf{S}_i\cdot\mathbf{S}_j\ . \quad (3.1)$$

Here, $\alpha N_0$ is the exchange constant of the interaction between localized spins $\{\mathbf{S}_i\}$ and that of the electron, $\mu_B$ is the Bohr magneton, $J_{ij}$ is the antiferromagnetic exchange constant between $Mn^{2+}$ ions, and $g$ and $g^*$ are the Landé $g$ factor of the $Mn^{2+}$ spins and of the electron, respectively. The second and third terms are the Zeeman interactions with the applied magnetic field. The first term leads to the large spin splittings of the electron levels underlying the large Faraday rotations in DMS's. The last term represents the antiferromagnetic interaction of the magnetic ions responsible for the low-temperature magnetic phases observed in DMS.

The Raman spectra of $Cd_{1-x}Mn_xTe$:Ga, $x=0.03$, are shown in Fig. 1 for the ($\hat{\boldsymbol{\sigma}}_+,\hat{\mathbf{z}}$) and ($\hat{\boldsymbol{\sigma}}_-,\hat{\mathbf{z}}$) polarization configurations with $T=40$ K and $H=60$ kG. The two Stokes features labeled PM and SF are present only in ($\hat{\boldsymbol{\sigma}}_+,\hat{\mathbf{z}}$), while the corresponding anti-Stokes features appear only in the ($\hat{\boldsymbol{\sigma}}_-,\hat{\mathbf{z}}$) configuration. The observed width of the PM line is instrument-limited, while that of the SF feature is $\sim 3$ cm$^{-1}$.

We have studied[31–33] the Raman line PM for several DMS systems and a large range of Mn concentrations. In the paramagnetic phase, the Raman shift $\omega_{PM}$ of this line varies linearly with $H$ and is independent of the temperature. The PM feature is associated with spin-flip transitions within the Zeeman multiplet of the $Mn^{2+}$ $3d$ electrons. Since the crystal-field splitting is too small to be observed in Raman scattering, the ground state of the $3d$ electrons can be treated as ${}^6S_{5/2}$. When a magnetic field is applied to the system, the sixfold degeneracy of this level is lifted. The resulting energy levels are given by $E(m_S)=g\mu_B Hm_S$, where $g\cong 2$ and $m_S$ is the spin projection along $\mathbf{H}$. The Stokes PM Raman line originates from the $\Delta m_S=+1$ spin-flip transitions between adjacent levels of this Zeeman multiplet with a Raman shift given by $\hbar\omega_{PM}=g\mu_B H$. Similarly, the anti-Stokes com-

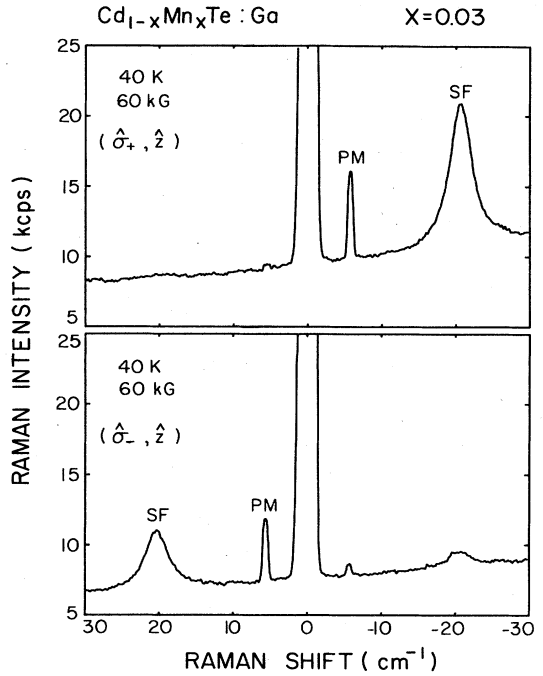


FIG. 1. Raman spectra of $Cd_{1-x}Mn_xTe$:Ga, $x=0.03$, showing the $\Delta m_S=\pm 1$ transitions within the Zeeman multiplet of $Mn^{2+}$ (PM) and the spin flip of electrons bound to Ga donors (SF). 1 kcps$\equiv 10^3$ counts/sec.

ponent is associated with the corresponding $\Delta m_S=-1$ spin-flip transitions. The Stokes line is observed in either the $(\hat{\sigma}_+,\hat{z})$ or $(\hat{z},\hat{\sigma}_-)$ polarization configurations, while the anti-Stokes component is present in either $(\hat{\sigma}_-,\hat{z})$ or $(\hat{z},\hat{\sigma}_+)$. Under conditions when the laser photon energy approaches that of the band gap, we observed[32] Raman features which can be attributed to multiples of the paramagnetic spin-flip transition ($\Delta m_S=\pm 2$), as well as to its combinations with longitudinal-optical (LO) phonons. The Stokes component of the Raman line at $2\omega_{PM}$ is observed in the $(\hat{\sigma}_+,\hat{\sigma}_-)$ polarization, while the anti-Stokes occurs in $(\hat{\sigma}_-,\hat{\sigma}_+)$. The combination of the spin-flip transition with the zone-center LO phonons[34] in $Cd_{1-x}Mn_xTe$ occurs with shifts of $\omega_{LO}\pm\omega_{PM}$ in the $(\hat{\sigma}_\pm,\hat{z})$ or $(\hat{z},\hat{\sigma}_\mp)$ configurations. Raman features with shifts of $3\omega_{PM}$, $4\omega_{PM}$, and $\omega_{LO}\pm 2\omega_{PM}$ have also been observed[33] in $Cd_{1-x}Mn_xTe$. Since the appearance of these features occurs only under band-gap resonance and the spin-flip—phonon combination modes involve only the LO phonons, and hence the Fröhlich interaction, an interband Raman mechanism was proposed.[32] This mechanism is based on a mutual spin-flip process between a band electron and a $Mn^{2+}$ ion attributed to the first term of Eq. (3.1) and provides an explanation for the polarization and resonance characteristics of the observed Raman features. The scattering cross section for this Raman mechanism is proportional to $(\alpha N_0)^2$, which is very strong in these alloys. In $Cd_{1-x}Mn_xTe$, for $x\gtrsim 0.30$, the PM line broadens and shifts as the temperature is lowered. As the antiferromagnetic phase is approached, the PM line evolves into one of the components of the magnon in an applied magnetic field.[32,34]

The SF feature of Fig. 1 is attributed to spin-flip Raman scattering from electrons bound to gallium donors. It has the same polarization characteristics as those of the PM line appearing[12] in the $(\hat{\sigma}_+,\hat{z})$ or $(\hat{z},\hat{\sigma}_-)$ polarizations for Stokes scattering and in $(\hat{\sigma}_-,\hat{z})$ or $(\hat{z},\hat{\sigma}_+)$ for anti-Stokes scattering. As illustrated in Fig. 2, the peak Raman shift of this spin-flip feature, $\tilde{\omega}$, exhibits a strong dependence on both temperature and magnetic field. The primary source of the spin splitting of the electronic level is the exchange coupling with the $Mn^{2+}$ ions [first term of Eq. (3.1)] with the Zeeman effect [second term of Eq. (3.1)] making a relatively small contribution. Hence, the Raman shift should be approximately proportional to the magnetization of the $Mn^{2+}$-ion system, which amplifies the effect of the magnetic field on the electron. As can be seen in Fig. 2, a finite Raman shift is observed for zero magnetic field. This effect is attributed by Dietl and Spałek[21] to the "bound magnetic polaron (BMP)": The electron localized on a donor in a diluted magnetic crystal polarizes the magnetic ions within its orbit, creating a spin cloud that exhibits a net magnetic moment. An additional effect on the binding energy of the electron bound to the donor originates from thermodynamic fluctuations of the magnetization and the resulting spin alignment of the magnetic ions around the donor.

### B. Spin-flip Raman scattering for low Mn concentration

As discussed in the preceding section, the spin splitting of the donor energy levels in DMS's has two sources, the magnetization of the $Mn^{2+}$ ions and the Zeeman effect. Due to the strong *s-d* coupling, the effects due to the magnetization will dominate. The Raman shift associated with spin-flip scattering from these donor states will have the form

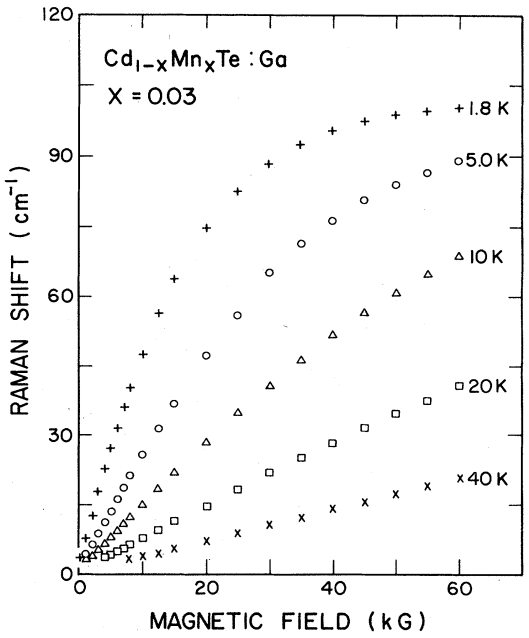


FIG. 2. Magnetic field and temperature dependence of the Raman shift associated with the spin flip of electrons bound to donors in $Cd_{1-x}Mn_xTe$:Ga, $x=0.03$.

$$\hbar\omega_0=\Delta_0=\frac{\alpha}{g\mu_B}M_0(H)+g^*\mu_B H\ , \tag{3.2}$$

where $M_0$ is the macroscopic magnetization. The magnetization will be proportional to the thermal average of the $Mn^{2+}$ spin projection along **H** multiplied by the density of $Mn^{2+}$ ions that contribute to the magnetization, yielding

$$\Delta_0=\bar{x}\alpha N_0\langle S_z^{\mathrm{Mn}}\rangle+g^*\mu_B H\ . \tag{3.3}$$

Here $N_0$ is the density of cations and $\bar{x}$ is the concentration of $Mn^{2+}$ ions that contribute to the magnetization. For small $x$, the crystal is paramagnetic and the thermal average of the $Mn^{2+}$ spins is

$$\langle S_z^{\mathrm{Mn}}\rangle=\tfrac{5}{2}B_{5/2}(g\mu_B H/k_B T)\ , \tag{3.4}$$

where $B_{5/2}$ is the Brillouin function $B_J$ for $J=\frac{5}{2}$. The spin-flip Raman shifts for $Cd_{1-x}Mn_xTe$, $x=0.01$, are shown as a function of temperature and magnetic field in Fig. 3. This sample was not intentionally doped, yet it exhibits $n$-type properties due to the presence of unknown—"anonymous"—donors. A similar plot is shown for $Cd_{1-x}Mn_xSe$, $x=0.01$, in Fig. 4. Although these samples are very similar, the Raman shifts of the $Cd_{1-x}Mn_xTe$, $x=0.01$, sample appear to saturate for a slightly lower magnetic field. This small effect can be attributed to the difference in the signs of the intrinsic $g$ factors, that is, $g^*(\mathrm{CdTe})=-0.75$ and $g^*(\mathrm{CdSe})=0.52$. Once the magnetization due to the $Mn^{2+}$ ions has reached saturation, the Raman shifts for $Cd_{1-x}Mn_xSe$, $x=0.01$, will continue to increase with magnetic field, while those for $Cd_{1-x}Mn_xTe$, $x=0.01$, will decrease. The fits shown in both figures were generated using Eqs. (3.3) and (3.4)

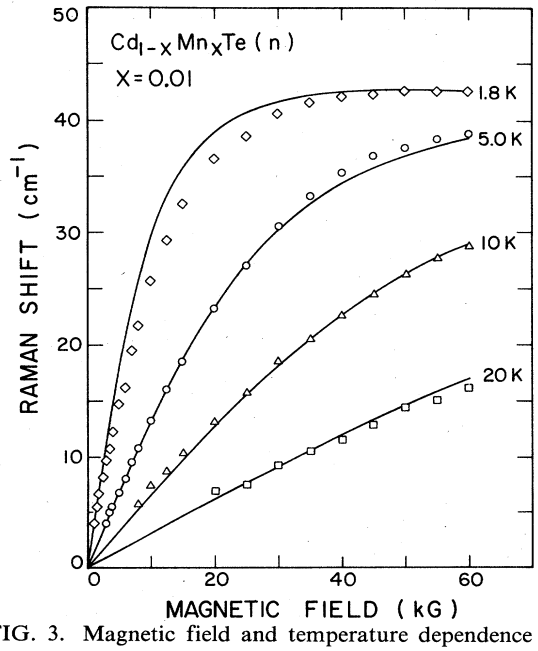


FIG. 3. Magnetic field and temperature dependence of the Raman shift associated with the spin flip of electrons bound to donors in $Cd_{1-x}Mn_xTe$, $x=0.01$. The theoretical curves result from Eqs. (3.3) and (3.4).

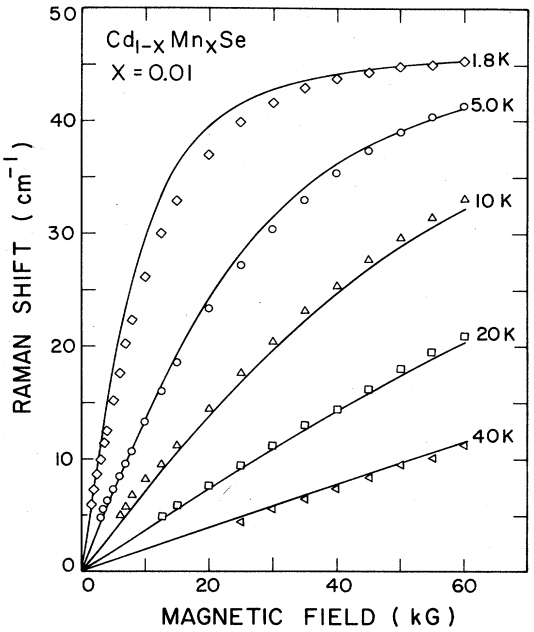


FIG. 4. Magnetic field and temperature dependence of the Raman shift associated with the spin flip of electrons bound to donors in $Cd_{1-x}Mn_xSe$, $x=0.01$. The theoretical curves result from Eqs. (3.3) and (3.4).

and the intrinsic $g$ factors of Table II. For $Cd_{1-x}Mn_xSe$, $x=0.01$, the effective Mn concentration is $\bar{x}=0.0084$, yielding $\bar{x}/x=0.70$, which indicates that, even for such a low value of the Mn concentration, a significant fraction of the magnetic ions do not contribute to the net magnetization due to effects of antiferromagnetic pairing. As can be seen in Figs. 3 and 4, the curves fit the experimental points quite well, except for those at $T=1.8$ K. For this temperature, the experimental points do not saturate as quickly as the theory predicts. Instead, it appears as if the temperature $T$ should be replaced by $T+T_{\mathrm{AF}}$, where $T_{\mathrm{AF}}$ is a phenomenological constant that is inserted to account for weak antiferromagnetic interactions. These deviations from the paramagnetic description, $T_{\mathrm{AF}}>0$ and $\bar{x}<x$, indicate that there is a significant antiferromagnetic coupling between the magnetic ions even for small $x$; such departures will clearly be more significant with increasing $x$.

### C. Compositional dependence of spin-flip Raman scattering: Mean-field approximation

The compositional dependence of spin-flip Raman scattering has two sources. Within a DMS system, such as $Cd_{1-x}Mn_xTe$, the properties of the spin splitting should show a strong dependence on the Mn concentration. For a given $x$, these properties should also vary from one DMS system to another, as illustrated by the spin-flip Raman shifts of $Cd_{1-x}Mn_xTe$:Ga, $Cd_{1-x}Mn_xSe$, and $Cd_{1-x}Mn_xS$ for $x=0.10$ shown in Figs. 5, 6, and 7. As given in Table I, the actual Mn concentrations in these three alloys are approximately the same, allowing some general observations from an intercomparison of these results.

TABLE II. Material parameters.

| Quantity | Symbol | $Cd_{1-x}Mn_xTe$ | $Cd_{1-x}Mn_xSe$ | $Cd_{1-x}Mn_xS$ |
|---|---|---|---|---|
| Intrinsic $g$ factor[a,b] | $g^*$ | $-0.75$ | 0.52 | 1.77 |
| Dielectric constant[a] | $\kappa$ | 10.9 | 10.6 | 8.9 |
| Effective mass[a] | $m^*/m_0$ | 0.11 | 0.13 | 0.20 |
| Exchange constant[c] (meV) | $\alpha N_0$ | 220 | 260 | 217 |

[a]For $x=0$ alloy.
[b]From Refs. 2 and 5.
[c]From Refs. 17, 35, and 36.

The above three samples were studied over the temperature range 1.8—40 K. In addition, the excellent Raman signals in $Cd_{1-x}Mn_xSe$ permitted observations for temperatures up to 160 K. At the higher temperatures, a significant number of the shallow donors are expected to be ionized, and the Raman scattering observed at these temperatures could be from both bound and thermally excited electrons. The spin-flip energies of these alloys deviate significantly from the paramagnetic behavior observed in alloys with small Mn concentrations as illustrated in Figs. 3 and 4. Such deviation is much more significant for the $Cd_{1-x}Mn_xTe$ sample, indicating that the antiferromagnetic temperature $T_{AF}$ should be significantly higher than those for the $Cd_{1-x}Mn_xSe$ and $Cd_{1-x}Mn_xS$ samples. The saturation Raman shift is largest in $Cd_{1-x}Mn_xSe$ due to the substantially larger $s$-$d$ exchange coupling $\alpha N_0$. All three samples show experimental evidence for the bound magnetic polaron, with zero-field shifts of $\sim 6$ $cm^{-1}$ for the $Cd_{1-x}Mn_xTe$, 9 $cm^{-1}$ for the $Cd_{1-x}Mn_xSe$, and 17.2 $cm^{-1}$ for the $Cd_{1-x}Mn_xS$ samples at $T=1.8$ K. These variations in the BMP energy are discussed in a subsequent section.

In the light of the various magnetic phases exhibited by diluted magnetic semiconductors, an important aspect of spin-flip Raman scattering is its dependence on the Mn concentration. The DMS systems $Cd_{1-x}Mn_xTe$ and $Cd_{1-x}Mn_xSe$ were studied over the range $0.01 \leq x \leq 0.30$, exceeding the concentration required for the onset of lattice frustration and the spin-glass phase.

The spin-flip Raman shifts for $Cd_{1-x}Mn_xTe$ at $T=1.8$ K are shown in Fig. 8 as a function of magnetic field and composition. The results for $x=0.01$ show the saturation behavior characteristic of the paramagnetic phase. As the Mn concentration is increased to $x=0.03$ and 0.05, the Raman shifts increase and the effects of saturation are still clearly evident, but less pronounced. For $x=0.10$, the deviation from the paramagnetic behavior is quite evident. For $H=60$ kG, the Raman shift for $x=0.10$ is only 4 times that for $x=0.01$. As $x$ exceeds 0.10, the Raman shifts for a given field actually decrease; note that the shifts for the $x=0.20$ sample lie below those for the $x=0.10$ sample, and the Raman shifts for the $Cd_{1-x}Mn_xTe$:Ga, $x=0.30$, sample are significantly smaller than those for the $x=0.10$ and 0.20 samples. When the temperature is raised to 20 K, the Raman shifts show a different dependence on the Mn concentration. As illustrated in Fig. 9, the Raman shifts show an approximately linear dependence on the magnetic field, a charac-

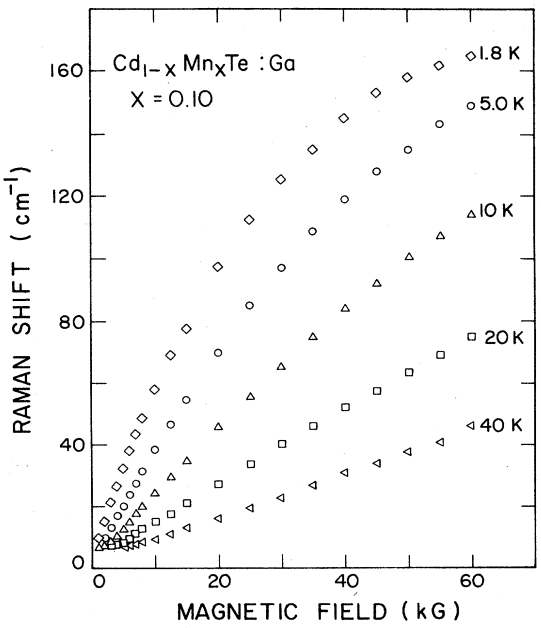


FIG. 5. Magnetic field and temperature dependence of the peak spin-flip Raman shift in the $Cd_{1-x}Mn_xTe$:Ga, $x=0.10$, sample.

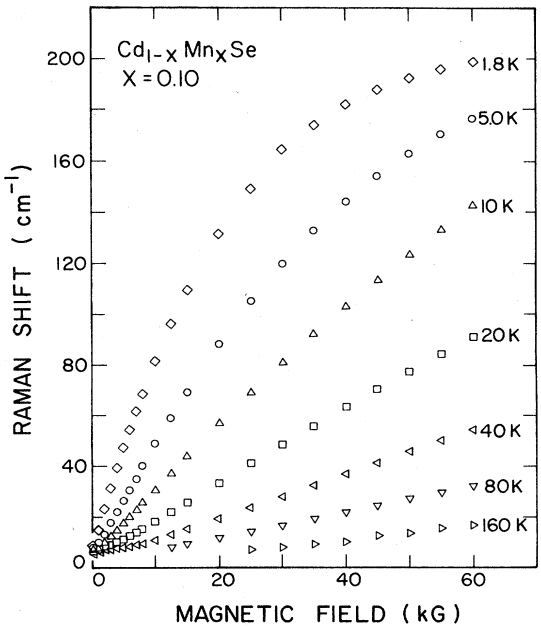


FIG. 6. Magnetic field and temperature dependence of the peak spin-flip Raman shift in the $Cd_{1-x}Mn_xSe$, $x=0.10$, sample.

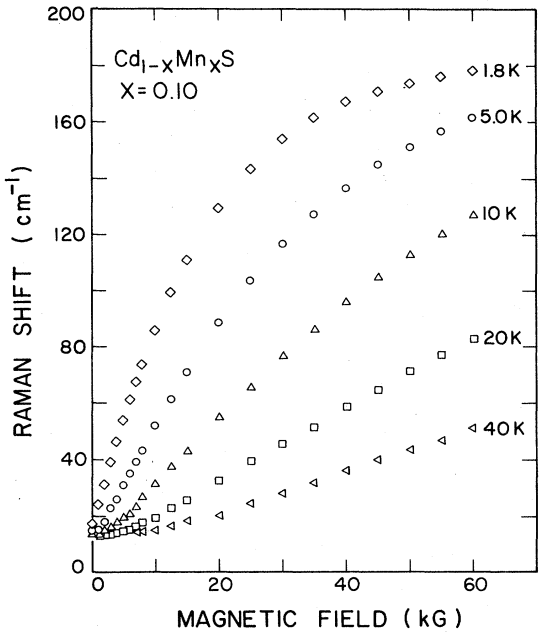


FIG. 7. Magnetic field and temperature dependence of the peak spin-flip Raman shift in the $Cd_{1-x}Mn_xS$, $x=0.10$, sample.

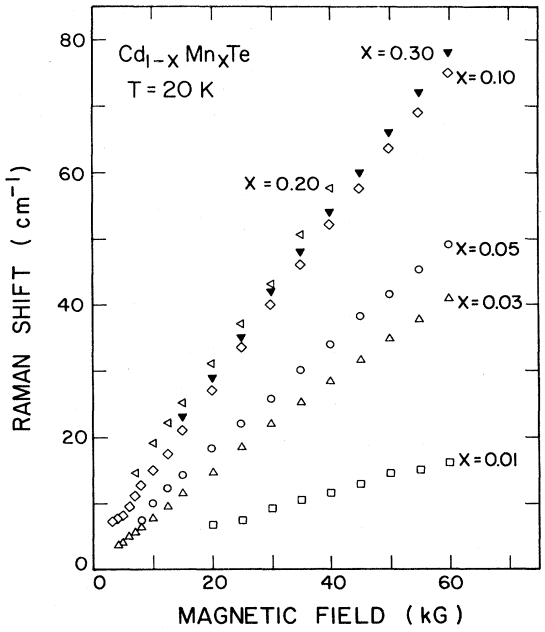


FIG. 9. Magnetic field and composition dependence of the peak spin-flip Raman shift in the $Cd_{1-x}Mn_xTe$ samples at $T=20$ K.

teristic of the high temperature, and increase with increasing $x$ until $x\simeq 0.25$. The Raman shifts for the $x=0.30$ sample now lie above those for $x=0.10$, yet still below those for the $x=0.20$ sample.

For $Cd_{1-x}Mn_xSe$, the situation is slightly different. As illustrated in Fig. 10, for $T=1.8$ K, the Raman shifts increase with Mn concentration and exhibit saturation effects for $x\leq 0.10$. The shifts for the nominally $x=0.20$ sample are essentially the same as those for the $x=0.10$ sample, reflecting the actual composition of the former, viz., $x\simeq 0.13$. As was the case for $Cd_{1-x}Mn_xTe$, the Raman shifts for the $x=0.30$ sample are significantly smaller than those for the $x=0.05$, 0.10, and 0.20 samples. Since spin-flip Raman scattering was observable at 40 K for all the $Cd_{1-x}Mn_xSe$ samples, it is possible to consider the Mn-concentration dependence of the Raman shifts at this temperature. As can be seen in Fig. 11, the Raman shifts increase with increasing $x$ for $x\leq 0.30$, although the rate of this increase becomes less for $x>0.10$.

Using the mean-field approximation, one can obtain an estimate of the antiferromagnetic temperature $T_{AF}$ and the effective Mn concentration $\bar{x}$. From these parameters, the temperature and composition dependence of the Raman shifts, as illustrated in Figs. 8—11, can be described in a more quantitative manner. In the mean-field approx-

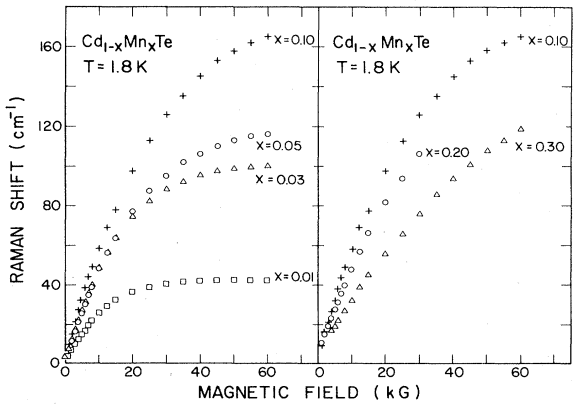


FIG. 8. Magnetic field and composition dependence of the peak spin-flip Raman shift in the $Cd_{1-x}Mn_xTe$ samples at $T=1.8$ K.

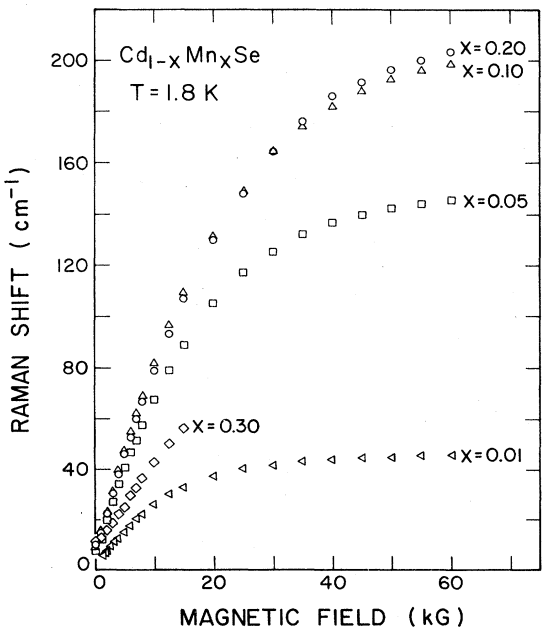


FIG. 10. Magnetic field and composition dependence of the peak spin-flip Raman shift in the $Cd_{1-x}Mn_xSe$ samples at $T=1.8$ K.

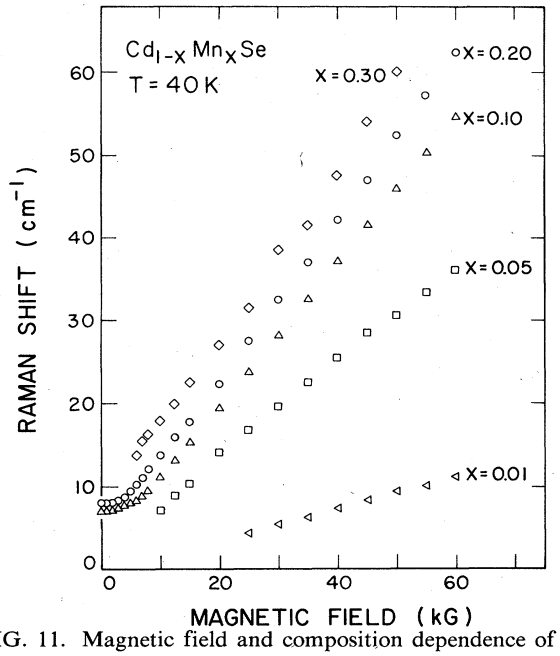


FIG. 11. Magnetic field and composition dependence of the peak spin-flip Raman shift in the $Cd_{1-x}Mn_xSe$ samples at $T=40$ K.

imation, we neglect the BMP energy and consider only those portions of the Raman-shift data that are linear in the magnetic field. In this approximation,

$$\Delta_x=\frac{\alpha}{g\mu_B}M_0(H)\simeq\frac{35\bar{x}(\alpha N_0)}{12k_B(T+T_{\rm AF})}g\mu_B H\ . \tag{3.5}$$

Hence, the effective $g$ is

$$g_{\rm eff}\equiv\frac{1}{\mu_B}\frac{\partial\Delta_0}{\partial H}\cong\frac{35\bar{x}(\alpha N_0)}{12k_B(T+T_{\rm AF})}g+g^*=g_x+g^*\ . \tag{3.6}$$

In order to determine $\bar{x}(\alpha N_0)$ and $T_{\rm AF}$ for each sample, the inverse slopes of the $\Delta_x$-versus-$H$ curves as determined by least-squares fits are plotted in Figs. 12 and 13 for the $Cd_{1-x}Mn_xTe$ and $Cd_{1-x}Mn_xSe$ samples, respectively. All the samples show a linear dependence given by

$$\left[\frac{\partial\Delta_x}{\partial H}\right]^{-1}=m(T+T_{\rm AF})\ \text{ for } T\le 20\ \text{K}\ .$$

From these plots, a least-squares fit was used to determine $T_{\rm AF}$ and $m\propto(\bar{x}\alpha N_0)^{-1}$. These results are summarized in Table III.

The parameters $\bar{x}\alpha N_0$ and $T_{\rm AF}$ listed in Table III exhibit some general trends. As expected, $\bar{x}\alpha N_0$ and $T_{\rm AF}$ increase with $x$ within a given DMS system. We note that $\bar{x}\alpha N_0$ does not increase linearly with $x$, reflecting a decreasing $\bar{x}/x$, for increasing $x$. The antiferromagnetic temperature $T_{\rm AF}$ shows a gradual increase with $x$ up to $x\simeq 0.25$; when $x$ exceeds this value there is clearly a dramatic increase in $T_{\rm AF}$ that can be attributed to effects of the spin-glass phase. For comparable compositions, one notices that the $Cd_{1-x}Mn_xTe$ values for $\bar{x}\alpha N_0$ are significantly smaller and the values for $T_{\rm AF}$ are substantially larger than those for $Cd_{1-x}Mn_xSe$. For

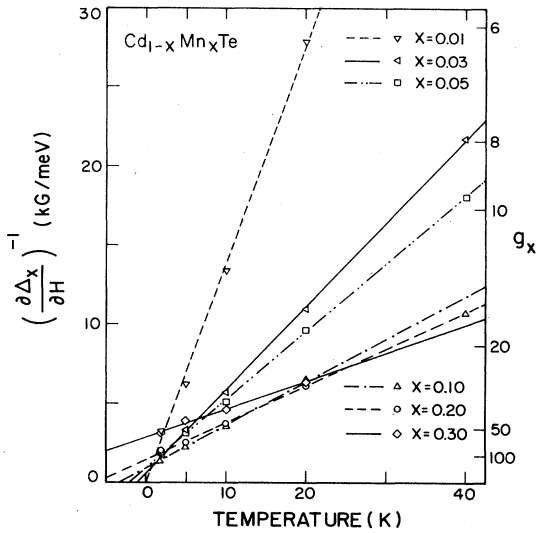


FIG. 12. $(\partial\Delta_x/\partial H)^{-1}$ vs temperature for $Cd_{1-x}Mn_xTe$. $\partial\Delta_x/\partial H$ is the slope of the linear portion of the Raman-shift—vs—$H$ data, corrected for the Zeeman contribution. The straight lines are fits to the experimental data. See Table III for parameters.

$Cd_{1-x}Mn_xS$ both $\bar{x}\alpha N_0$ and $T_{\rm AF}$ are smaller than for $Cd_{1-x}Mn_xSe$. These trends reflect the relative strengths of the $s$-$d$ exchange coupling $\alpha N_0$ and of the antiferromagnetic interaction of the $Mn^{2+}$ ions, as manifested in $\bar{x}/x$ and $T_{\rm AF}$.

We note from Fig. 13 that the data at $T=40$ K lie slightly below the straight-line fits, indicating a possible temperature dependence in the slope of $(\partial\Delta_x/\partial H)^{-1}$. We studied this effect in more detail in $Cd_{1-x}Mn_xSe$ for the $x=0.10$ and 0.20 samples, since spin-flip scattering was observed in these samples up to $T=160$ and 80 K, respectively. In Fig. 14 we present the temperature dependence

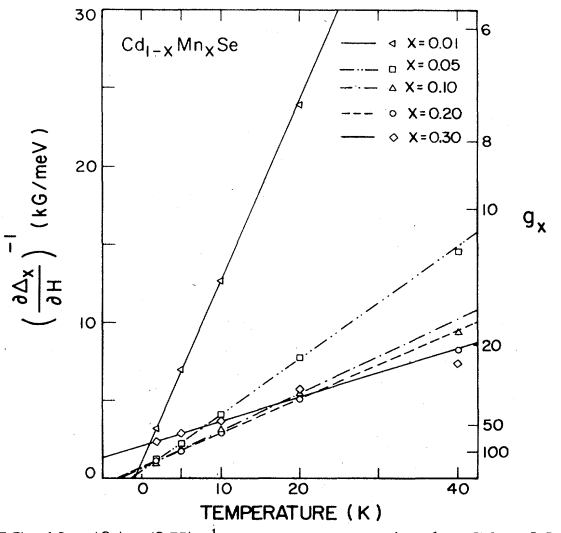


FIG. 13. $(\partial\Delta_x/\partial H)^{-1}$ vs temperature in the $Cd_{1-x}Mn_xSe$ samples. $\partial\Delta_x/\partial H$ is the slope of the linear portion of the Raman-shift—vs—$H$ data, corrected for the Zeeman contribution. The straight lines are fits to the experimental data. See Table III for parameters.

TABLE III. Mean-field parameters.

| DMS system | Mn concentration ($x$) Nominal | Measured | $\bar{x}\alpha N_0$ (meV) | $T_{AF}$ (K) | Temperature range (K) |
|---|---|---|---|---|---|
| $Cd_{1-x}Mn_xTe$ | 0.01 | | 2.03 | 0.43 | $\lesssim 20$ |
| | 0.03 | 0.035 | 4.85 | 1.14 | $\lesssim 40$ |
| | 0.05 | 0.044 | 5.95 | 2.25 | $\lesssim 40$ |
| | 0.10 | 0.102 | 9.43 | 3.37 | $\lesssim 20$ |
| | 0.20 | 0.250 | 11.0 | 6.24 | $\lesssim 20$ |
| | 0.30 | 0.295 | 14.4 | 16.2 | $\lesssim 20$ |
| $Cd_{1-x}Mn_xSe$ | 0.01 | 0.012 | 2.18 | 0.85 | $\lesssim 40$ |
| | 0.05 | 0.051 | 7.06 | 1.38 | $\lesssim 20$ |
| | 0.10 | 0.104 | 10.1 | 2.28 | $\lesssim 20$ |
| | 0.20 | 0.129 | 11.5 | 3.10 | $\lesssim 20$ |
| | 0.30 | 0.311 | 16.2 | 13.3 | $\lesssim 40$ |
| $Cd_{1-x}Mn_xS$ | 0.02 | 0.022 | 3.17 | 0.53 | $\lesssim 20$ |
| | 0.10 | 0.125 | 8.36 | 1.60 | $\lesssim 20$ |

of $(\partial\Delta_x/\partial H)^{-1}$ for the entire temperature ranges. The solid lines are the same as those in Fig. 13, whereas the dashed curves represent least-squares fits to the second-order polynomial $p+qT+rT^2$, where the deviation from the linear relationship is expressed by the quadratic term. The decreasing slope of $(\partial\Delta_x/\partial H)^{-1}$ is indicative of $\bar{x}$ increasing and/or $T_{AF}$ decreasing with $T$; both are possible due to the weakening of the antiferromagnetic coupling with temperature.

### D. The bound magnetic polaron

In order to discuss the experimental results on the bound magnetic polaron, it is useful to review the theory for it as developed by Dietl and Spałek.[20,21] The electron is assumed to be bound to a shallow donor and interacting through an $s$-$d$ coupling with a paramagnetic subsystem of localized magnetic moments. Only the large-polaron case is considered, allowing the continuous-medium, effective-mass, and molecular-field approximation. This model assumes that the donor electron interacts with a large cloud of spins with an effective classical spin.

Neglecting field-induced anisotropy, Dietl and Spałek derive an effective BMP Hamiltonian given by

$$H(\boldsymbol{\Delta})=-k_BT\ln\left[2\cosh\left[\frac{\Delta}{2k_BT}\right]\right]+\frac{(\boldsymbol{\Delta}-\boldsymbol{\Delta}_0)^2}{8\epsilon_p}+E_D(a)\,, \tag{3.7}$$

where $E_D(a)$ is the binding energy of the electron arising from the Coulomb part, $\Delta$ is the magnitude of the spin splitting with $\boldsymbol{\Delta}$, parallel to the effective local magnetic field, defining the direction of the spin-quantization axis of the electron,

$$\boldsymbol{\Delta}_0=\frac{\alpha}{g\mu_B}\mathbf{M}_0+g^*\mu_B\mathbf{H} \tag{3.8}$$

is the magnetic-field-induced component of $\boldsymbol{\Delta}$, and

$$\epsilon_p=\frac{\alpha^2\chi}{32\pi a^3(g\mu_B)^2} \tag{3.9}$$

is the characteristic BMP energy for an $s$-type wave function with an effective Bohr radius $a$. Here, $\mathbf{M}_0$ is the magnetic-field-induced magnetization and $\chi$ is the magnetic susceptibility. At a finite temperature a range of $\boldsymbol{\Delta}$ beyond the minimum of $H(\boldsymbol{\Delta})$ is accessible to the system. The probability of a thermal fluctuation of the magnetization giving rise to a specific $\boldsymbol{\Delta}$ is

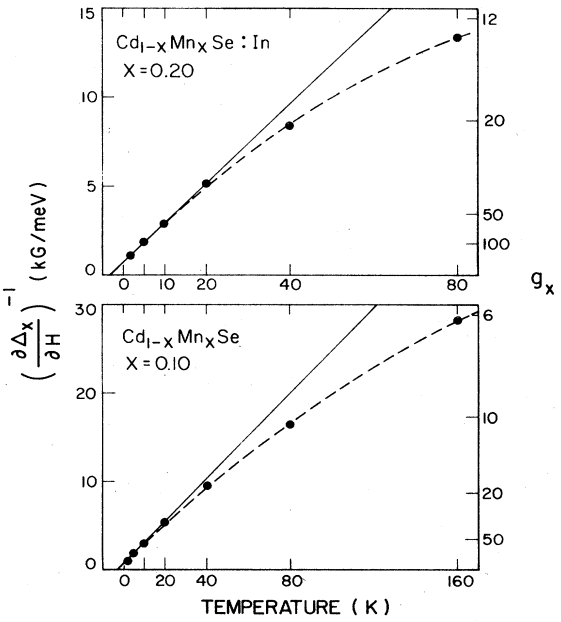


FIG. 14. $(\partial\Delta_x/\partial H)^{-1}$ vs temperature in the $Cd_{1-x}Mn_xSe$, $x=0.10$ and 0.20, samples. The straight lines are fits to the experimental data for $T\lesssim 20$ K. The dashed curves are fits of the form $(\partial\Delta_x/\partial H)^{-1}=p+qT+rT^2$, where $p=0.832$ (0.715) kG/meV, $q=0.224$ (0.229) kG/meV K, and $r=-0.335$ $(-0.889)\times10^{-3}$ kG/meV K$^2$ for the $x=0.10$ (0.20) sample.

$$P(\Delta)=C\exp\left[-\frac{H(\Delta)}{k_BT}\right], \tag{3.10}$$

where $C$ is a normalization constant.

The probability distribution for $\Delta=|\boldsymbol{\Delta}|$, $P(\Delta)$, is given by integrating (3.10) over all angles, yielding

$$P(\Delta)=C'\Delta\sinh\left[\frac{\Delta\Delta_0}{4\epsilon_pk_BT}\right]\times\cosh\left[\frac{\Delta}{2k_BT}\right]\exp\left[-\frac{\Delta^2}{8\epsilon_pk_BT}\right]. \tag{3.11}$$

In the absence of a magnetic field, $P(\Delta)$ reduces to

$$P(\Delta)\,|_{H=0}=C''\Delta^2\exp\left[-\frac{\Delta^2}{8\epsilon_pk_BT}\right]\cosh\left[\frac{\Delta}{2k_BT}\right], \tag{3.12}$$

where

$$C''^{-1}=\frac{1}{4\pi}(8\pi\epsilon_pk_BT)^{3/2}\left[1+\frac{\epsilon_p}{k_BT}\right]\exp\left[\frac{\epsilon_p}{2k_BT}\right]. \tag{3.13}$$

The theory of Dietl and Spałek results in an intensity distribution characterizing the spin-flip Raman line, $I(\Delta)$, to be $P(\Delta)$, given by Eqs. (3.11) or (3.12), multiplied by the probability that the donor electron has its spin aligned parallel (antiparallel) to the effective field $\boldsymbol{\Delta}(H,T)$,

$$I(\Delta)=\overline{C}P(\Delta)\exp\left[\pm\frac{\Delta}{2k_BT}\right]\left[2\cosh\left[\frac{\Delta}{2k_BT}\right]\right]^{-1}, \tag{3.14}$$

where $\overline{C}$ is a constant related to the scattering cross section, and $\pm$ refers to the Stokes and anti-Stokes components of the line. The peak position of the Raman line, $\tilde{\Delta}$, satisfies

$$\tilde{\Delta}^2\mp2\epsilon_p\tilde{\Delta}-\tilde{\Delta}\Delta_0\coth\left[\frac{\tilde{\Delta}\Delta_0}{4\epsilon_pk_BT}\right]-4\epsilon_pk_BT=0, \tag{3.15}$$

which shows an asymmetry in $\tilde{\Delta}$ between the Stokes and anti-Stokes components. The final expression for the Raman intensity as calculated by Dietl and Spałek[21] and Heiman *et al.*[16] does not include the effects of the magnetic field and temperature on the matrix elements of the Raman tensor. Since Raman scattering proceeds through intermediate states, the Raman matrix elements exhibit an angular dependence such that the cross section for scattering from a donor electron with a given $\boldsymbol{\Delta}$ depends not just on $|\boldsymbol{\Delta}|$ as implicit in Eq. (3.14), but also on the angle between $\boldsymbol{\Delta}$ and $\boldsymbol{\Delta}_0||\mathbf{H}$. This angular dependence has a small effect on the peak position $\tilde{\Delta}$. However, in light of the approximations that made the problem tractable and lead to the result of Eq. (3.7), this small correction can be neglected and Eq. (3.15) serves as a good approximation for $\tilde{\Delta}$. However, the angular dependence of the Raman matrix elements needs to be considered in determining the magnetic field and temperature dependence of the polarization characteristics of the spin-flip Raman feature. This is discussed in more detail in subsection E.

In order to calculate $\tilde{\Delta}$, the magnetic-field-induced spin splitting $\Delta_0$ and the characteristic energy of the bound magnetic polaron, $\epsilon_p$, must first be determined. For a weakly antiferromagnetic system,

$$\Delta_0\cong\bar{x}\alpha N_0\tfrac{5}{2}B_{5/2}(\eta)+g^*\mu_BH, \tag{3.16}$$

where

$$\eta=\frac{g\mu_BH}{k_B(T+T_{\rm AF})}, \tag{3.17}$$

and

$$\epsilon_p=\frac{3}{14}\frac{W_0^2}{k_B(T+T_{\rm AF})}\frac{\partial}{\partial\eta'}B_{5/2}(\eta')\Big|_{\eta'=\eta}, \tag{3.18}$$

where we use the notation of Heiman *et al.*,[16]

$$W_0^2=\frac{35}{96}\frac{\bar{x}(\alpha N_0)^2}{\pi a^3N_0}. \tag{3.19}$$

As demonstrated by Dietl and Spałek,[21] the dependence of the effective Bohr radius ($a$) on $\bar{x}$, $T_{\rm AF}$, $H$, and $T$ can be determined using a variational technique. The values of the effective mass $m^*$ and the static dielectric constant $\kappa$ are needed in order to evaluate the radius $a$ using this procedure. Since the effects of composition on these parameters are not known, only an approximate value for $a$ can be deduced. Therefore, in generating the theoretical fits to be discussed here, it is convenient to treat $W_0$, and hence $a$, as a third adjustable parameter along with $\bar{x}$ and $T_{\rm AF}$. The resulting values of $a$ may then be compared with the known Bohr radii for $x=0$.

The spin-flip Raman shifts are plotted in Fig. 15 as a function of magnetic field and temperature for $Cd_{1-x}Mn_xS$, $x=0.02$. The data clearly exhibit a strong saturation tendency for this magnetic field range, indicative of a weak antiferromagnetic system. The donor levels in this sample exhibit a zero-field spin splitting of $\sim9$ $cm^{-1}$ for $T=1.8$ K. The curves in this figure are the best fits generated from Eqs. (3.15), (3.16), and (3.18), yielding $\bar{x}\alpha N_0=3.75$ meV, $T_{\rm AF}=0.88$ K, and $W_0=0.53$ meV. For this weak antiferromagnetic sample, the theory gives an excellent description for the entire temperature and magnetic field ranges. As can be seen, the only significant discrepancy between the theory and the experimental results occurs at very low magnetic fields.

For larger Mn concentrations the antiferromagnetic coupling between magnetic ions becomes more important. For the higher compositions, the theory was used to fit the data at only low magnetic fields. In the mean-field approximation, the magnetic-field-induced spin splitting can then be approximated by

$$\Delta_0\cong\tfrac{35}{12}\bar{x}\alpha N_0\frac{g\mu_BH}{k_B(T+T_{\rm AF})}+g^*\mu_BH, \tag{3.20}$$

and the characteristic BMP energy becomes magnetic field independent, i.e.,

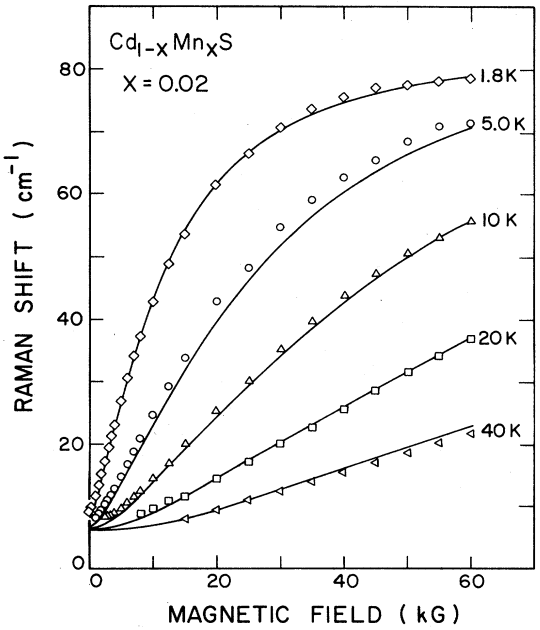


FIG. 15. Magnetic field and temperature dependence of the peak spin-flip Raman shift in the $Cd_{1-x}Mn_xS$, $x=0.02$, sample. The best-fit curves were generated from Eqs. (3.15)–(3.19) with $\bar{x}\alpha N_0=3.75$ meV, $T_{AF}=0.88$ K, and $W_0=0.53$ meV.

$$\epsilon_p \cong \frac{W_0^2}{4k_B(T+T_{AF})} . \tag{3.21}$$

The low-field data and the associated theoretical curves are plotted in Fig. 16 for $Cd_{1-x}Mn_xTe$:Ga, $x=0.03$, 0.05, and 0.10. As can be seen in Fig. 16(a), a zero-field shift of 3.5 $cm^{-1}$ was observed in $Cd_{1-x}Mn_xTe$:Ga, $x=0.03$, at $T=1.8$ K. The data for the other two samples, $x=0.05$ and 0.10, give evidence of zero-field shifts of $\sim 4$ and $\sim 6$ $cm^{-1}$. Although the Mn concentrations of the $Cd_{1-x}Mn_xTe$ samples are larger than that of the $Cd_{1-x}Mn_xS$ sample of Fig. 15, the zero-field spin splittings are much smaller. The theoretical fits were generated with the parameters listed in Table IV. The resulting curves describe the magnetic field and temperature dependence of the data well, particularly for $x=0.10$. For this sample, the most significant discrepancy between the theoretical and experimental results occurs for $T=40$ K and can be traced to the temperature dependence exhibited by $\bar{x}$ and $T_{AF}$ for $T>40$ K, as discussed in subsection C. From Eq. (3.15), the Stokes Raman shift of the peak position of the zero-field spin-flip transition is given by

$$\tilde{\Delta}=\epsilon_p+(\epsilon_p^2+8\epsilon_p k_B T)^{1/2} . \tag{3.22}$$

The nature of the temperature dependence of $\tilde{\Delta}$ can be determined by evaluating the slope of $\tilde{\Delta}$ versus $T$ at $T=0$. Thus,

$$\left.\frac{\partial\tilde{\Delta}}{\partial T}\right|_{T=0}=2\left[2k_B-\frac{\epsilon_p(0)}{T_{AF}}\right]$$

$$\text{is}\begin{cases}<0 & \text{if } W_0>\sqrt{8}k_B T_{AF} ,\\ >0 & \text{if } W_0<\sqrt{8}k_B T_{AF} .\end{cases} \tag{3.23}$$

The condition $W_0<\sqrt{8}k_B T_{AF}$ describes a situation in which the antiferromagnetic couping manifested in $T_{AF}$ is stronger than the tendency of the donor electron to induce a net magnetic moment in the spin cloud. For the $Cd_{1-x}Mn_xTe$(Ga), $x=0.10$, sample, having $W_0=0.51$ meV and $\sqrt{8}k_B T_{AF}=0.72$ meV, the theory predicts that the zero-field shift will increase with temperature. The curves in Fig. 16(c) generated with these parameters describe the data well, but the lack of zero-field data does not allow a confirmation of the predicted zero-field behavior. Similar comments apply to Fig. 16(b).

The low-field data for the $Cd_{1-x}Mn_xSe$, $x=0.05$, 0.10, 0.20, and 0.30, samples are shown in Fig. 17. The zero-field Raman shifts for $T=1.8$ K vary from $\sim 7$ $cm^{-1}$ for $x=0.05$ to $\sim 12$ $cm^{-1}$ for $x=0.30$. In contrast to $Cd_{1-x}Mn_xTe$, the larger shifts permit a detailed study of the zero-field Raman feature over a wide range of Mn concentration and temperature. The adjustable parameters used to generate the best fits in Fig. 17 are given in Table IV. The theoretical curves of Figs. 17(a)–17(c) describe the measured Raman shifts very well except for

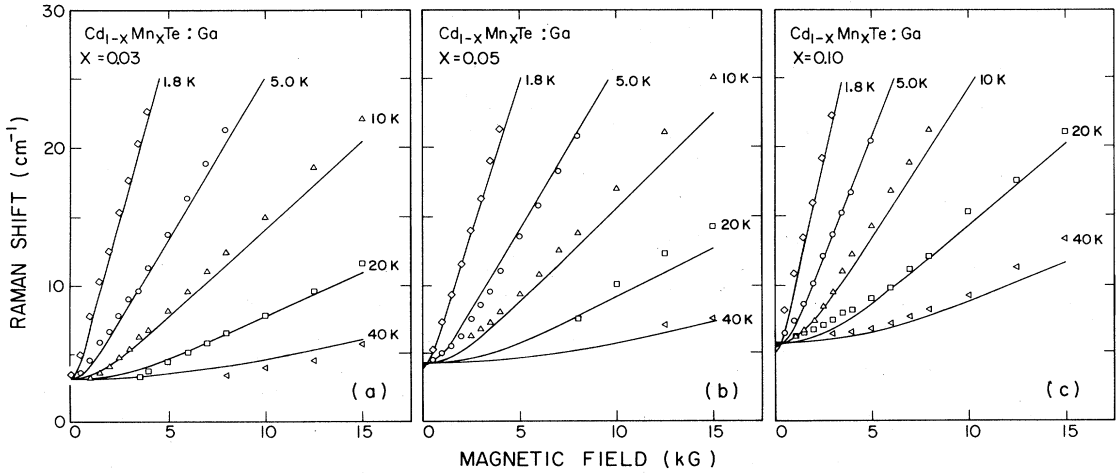


FIG. 16. Magnetic field and temperature dependence of the peak spin-flip Raman shift in the $Cd_{1-x}Mn_xTe$:Ga, $x=0.05$, 0.10, and 0.20, samples at low fields. The best-fit curves were generated from Eqs. (3.15), (3.20), and (3.21). See Table IV for parameters.

TABLE IV. Parameters for theoretical fits to the BMP. (Values of $T_{AF}$ and $W_0$ in parentheses result from zero-field fits.)

| DMS system | Mn concentration ($x$) Nominal | Measured | $\bar{x}\alpha N_0$ (meV) | $T_{AF}$ (K) | $W_0$ (meV) | $\bar{x}/x$ |
|---|---|---|---|---|---|---|
| $Cd_{1-x}Mn_xTe$ | 0.03 | 0.035 | 4.85 | 1.09 | 0.28 | 0.63 |
| | 0.05 | 0.044 | 5.70 | 2.08 | 0.38 | 0.59 |
| | 0.10 | 0.102 | 9.45 | 2.96 | 0.51 | 0.42 |
| | 0.20 | 0.250 | 13.55 | 6.88 | 0.77 | 0.25 |
| | 0.30 | 0.295 | 15.20 | 16.55 | 1.10 | 0.23 |
| $Cd_{1-x}Mn_xSe$ | 0.05 | 0.051 | 7.80 | 1.65 (1.16) | 0.58 (0.53) | 0.59 |
| | 0.10 | 0.104 | 10.10 | 2.20 (1.28) | 0.67 (0.63) | 0.37 |
| | 0.20 | 0.129 | 11.75 | 2.82 (1.50) | 0.73 (0.68) | 0.35 |
| | 0.30 | 0.311 | 13.85 | 9.84 (4.04) | 1.24 (1.04) | 0.17 |
| $Cd_{1-x}Mn_xS$ | 0.02 | 0.022 | 3.75 | 0.88 | 0.53 | 0.79 |
| | 0.10 | 0.125 | 9.10 | 1.88(1.88) | 1.04(1.04) | 0.34 |

very low magnetic fields and for temperatures above 20 K. For the $x=0.10$ and 0.20 samples, the measured zero-field spin splittings exhibit a much stronger temperature dependence than predicted by the theory using the best-fit parameters of Table IV. The Mn concentration of the $Cd_{1-x}Mn_xSe$:In, $x=0.30$, sample is well above the percolation threshold, and hence, the antiferromagnetic coupling in it is very significant. The theory does not describe the temperature dependence of the spin splittings well, especially for very low fields. Based on the values of $\bar{x}$, $T_{AF}$, and $W_0$ determined from the best fit of Eqs. (3.15), (3.20), and (3.21) to the experimental results, the theory predicts a strong temperature dependence of the zero-field shifts, with the shifts increasing with increasing temperature. The data show a weaker temperature dependence, with the spin-flip energies decreasing rather than increasing with temperature.

In contrast to $Cd_{1-x}Mn_xTe$ and $Cd_{1-x}Mn_xSe$, the best fits generated from the theory predict the zero-field Raman shifts in the $Cd_{1-x}Mn_xS$, $x=0.10$, sample very well. As illustrated in Fig. 18, these curves give an excellent description of the measured magnetic field and temperature dependence for $T<20$ K. For $T\geq 20$ K, the fits are still very good, but, as in the other alloys, the difference between theory and experiment increases with temperature.

The above analysis demonstrates that the theory of Dietl and Spałek developed for paramagnetic or weakly antiferromagnetic systems does provide a very good description of spin-flip Raman scattering in the diluted magnetic semiconductors $Cd_{1-x}Mn_xTe$, $Cd_{1-x}Mn_xSe$, and $Cd_{1-x}Mn_xS$ for low Mn concentration ($x<0.15$). However, the parameters used in their theory appear to exhibit a temperature dependence for $T\gtrsim 40$ K and a magnetic field dependence for $H<2$ kG. For concentrations above the percolation threshold, as illustrated by the results for $Cd_{1-x}Mn_xSe$:In, $x=0.30$, the theory is not as successful. As in the mean-field description, the BMP-theory parameters listed in Table IV show some general trends: $\bar{x}/x$ decreases with $x$ and is comparable for different DMS's with the same Mn concentration; $W_0$ increases with $x$ and for comparable $x$ is largest for $Cd_{1-x}Mn_xS$ and smallest for $Cd_{1-x}Mn_xTe$; and $\bar{x}\alpha N_0$ and $T_{AF}$ are comparable to those determined using the mean-field approach of subsection C.

The BMP theory [see Eq. (3.15)] predicts an asymmetry in the peak Raman shift for the Stokes and anti-Stokes components of the Raman feature. The spectra for the $Cd_{1-x}Mn_xSe$:In, $x=0.20$, sample at $T=20$ K are shown in Fig. 19(a) for $H=0$ and in Fig. 19(b) for $H=10$ kG.

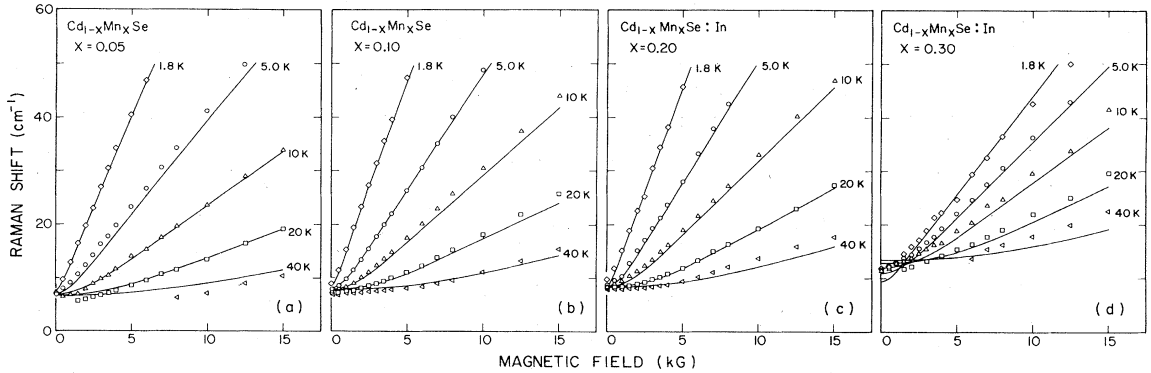


FIG. 17. Magnetic field and temperature dependence of the peak spin-flip Raman shift in the $Cd_{1-x}Mn_xSe$, $x=0.05$, 0.10, 0.20, and 0.30, samples at low fields. The best-fit curves were generated from Eqs. (3.15), (3.20), and (3.21). See Table IV for parameters.

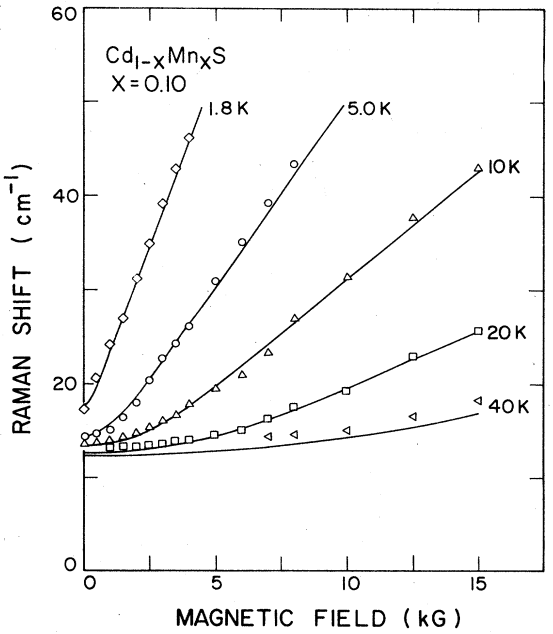


FIG. 18. Magnetic field and temperature dependence of the peak spin-flip Raman shift in the $Cd_{1-x}Mn_xS$, $x=0.10$, sample. The best-fit curves were generated from Eqs. (3.15), (3.20), and (3.21) with $\bar{x}\alpha N_0=9.10$ meV, $T_{AF}=1.88$ K, and $W_0=1.04$ meV.

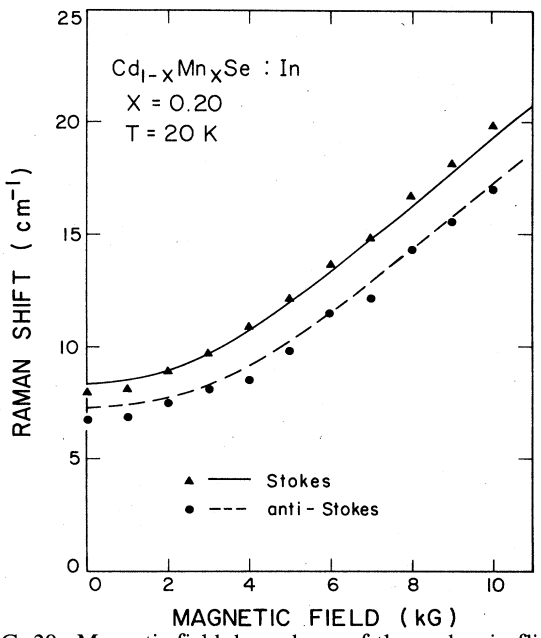


FIG. 20. Magnetic field dependence of the peak spin-flip Raman shift for Stokes and anti-Stokes scattering in the $Cd_{1-x}Mn_xSe$:In, $x=0.20$, sample at $T=20$ K. The theoretical curves were generated from Eqs. (3.15), (3.20), and (3.21), with $\bar{x}\alpha N_0=11.75$ meV, $T_{AF}=2.82$ K, and $W_0=0.73$ meV.

As can be seen, there is an observable difference in the peak Raman shifts of the Stokes and anti-Stokes components for both values of the magnetic field. This asymmetry results from the fact that the Stokes (anti-Stokes)

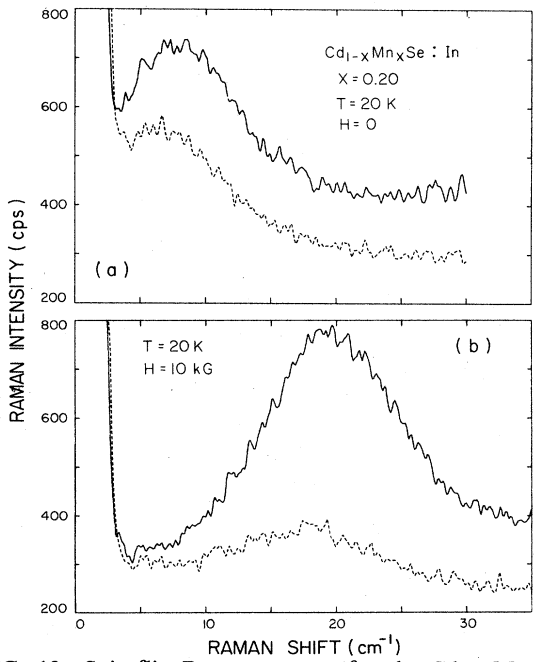


FIG. 19. Spin-flip Raman spectra for the $Cd_{1-x}Mn_xSe$:In, $x=0.20$, sample at $T=20$ K for $H=0$ and 10 kG. The solid (dashed) line is the Stokes (anti-Stokes) component. The scans were recorded in the $(\hat{x},\hat{z})$ polarization.

spin-flip Raman feature reflects the distribution of the spin splittings multiplied by the probability that the ground state (excited state) is occupied. The probability of the electron being in the excited state decreases with the magnitude of the spin splitting, and results in the peak Raman shift of the anti-Stokes feature being less than that of the Stokes feature. The measured Stokes and anti-Stokes peak Raman shifts are plotted in Fig. 20. The theoretical curves of this figure were generated with the same parameters as in Fig. 17(c). The predicted and measured results agree well, particularly in the magnitude of the asymmetry which increases slightly as the magnetic field is increased.

The zero-field spin-flip Raman spectra for the $Cd_{1-x}Mn_xSe$, $x=0.05$, 0.10, 0.20, and 0.30, samples at $T=1.8$ K are shown in Fig. 21. As can be seen in this figure, the shifts and widths of the Raman features increase with Mn concentration for a given temperature. The theoretical curves are best fits generated from Eqs. (3.12), (3.13), (3.14), and (3.21) with the peak intensities adjusted to match the experimental values. The values of the parameters $W_0$ and $T_{AF}$ that give these fits are listed in Table IV. As illustrated in the figure, the theory provides a very good description of the shape of the Raman feature for $x \lesssim 0.10$. The experimental spectra for the $Cd_{1-x}Mn_xSe$:In, $x=0.20$ and 0.30, samples show the Raman feature to have an additional width not predicted by the theory. A possible source of this additional width may be spatial fluctuations in the Mn concentration.

The zero-field spin-flip Raman spectra of the $Cd_{1-x}Mn_xSe$, $x=0.10$, sample are shown in Fig. 22 for $T=1.8$, 5, 10, and 20 K. As can be seen in the figure, the Raman shift of the spin-flip feature decreases for higher

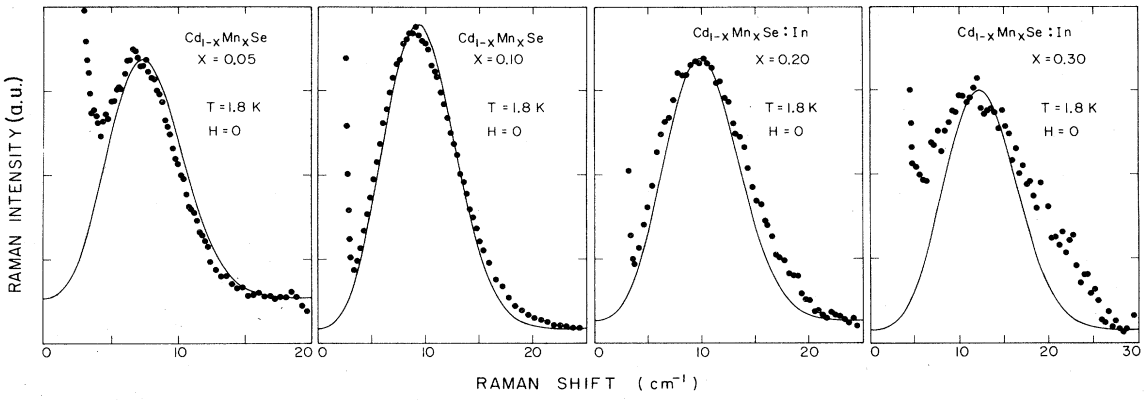


FIG. 21. Zero-field spin-flip Raman spectra for the $Cd_{1-x}Mn_xSe$, $x=0.05$, 0.10, 0.20, and 0.30, samples at $T=1.8$ K. The scans were recorded in the $(\hat{\sigma}_+,\hat{z})$ polarization. The best-fit curves were generated from Eqs. (3.12)—(3.14) with the peak intensities adjusted to match the experimental results. See Table IV for parameters. a.u. denotes arbitrary units.

temperatures. Other than for the temperature, the experimental conditions were identical for the four scans. The four theoretical curves are best fits generated from Eqs. (3.12), (3.13), (3.14), and (3.21) for $T_{AF}=1.28$ K and $W_0=0.63$ meV, using the same value for $\bar{C}$ in Eq. (3.14). The predicted variation of the peak intensity with temperature agrees quite well with the experimental results. Due to the excellent quality of the data for this particular sample, the observed small difference in the experimental and theoretical line shapes is real. We note that the Raman spectra in this figure are more asymmetric than the theory predicts.

The zero-field values of the parameters $T_{AF}$ and $W_0$ listed in Table IV for the $Cd_{1-x}Mn_xSe$ samples are significantly smaller than those determined from fitting the theory to the finite-field Raman shifts. As was discussed in the preceding section, the finite-field parameters did not describe the zero-field spin splittings well. The largest difference between the finite-field and zero-field values occur for $T_{AF}$, the latter being significantly smaller than the former. To a lesser extent, the values of $W_0$ are also smaller. The large discrepancy in the values of $T_{AF}$ indicates that this parameter exhibits a magnetic field dependence which appears to be most significant at very low magnetic fields.

The zero-field spin-flip Raman shifts in the $Cd_{1-x}Mn_xSe$ samples are plotted in Fig. 23 as a function of temperature. The theoretical curves of this figure were generated from Eqs. (3.21) and (3.22) using the zero-field parameters of Table IV and give a good description of the observed temperature dependence. We note that the striking temperature dependence of the zero-field spin splittings seen for low Mn concentrations weakens as $x$ is increased.

The zero-field spin-flip Raman spectrum for the $Cd_{1-x}Mn_xS$, $x=0.10$, sample at $T=1.8$ K is shown in Fig. 24. The Raman shift of $\sim 17$ cm$^{-1}$ is much larger than the shifts measured for $Cd_{1-x}Mn_xSe$ and $Cd_{1-x}Mn_xTe$ samples. The theoretical curve of Fig. 24 is a best fit to the data with $T_{AF}=1.88$ K and $W_0=1.04$ meV. These parameters are identical to the finite-field results. This is not surprising, since the finite-field fits for this sample did match the zero-field Raman shifts (see Fig. 18). The magnitude of the zero-field spin splitting is relatively large, and the variation of the Raman shift with temperature shown in Fig. 25 is more pronounced than that for $Cd_{1-x}Mn_xSe$.

In comparing the theory with the experimental results,

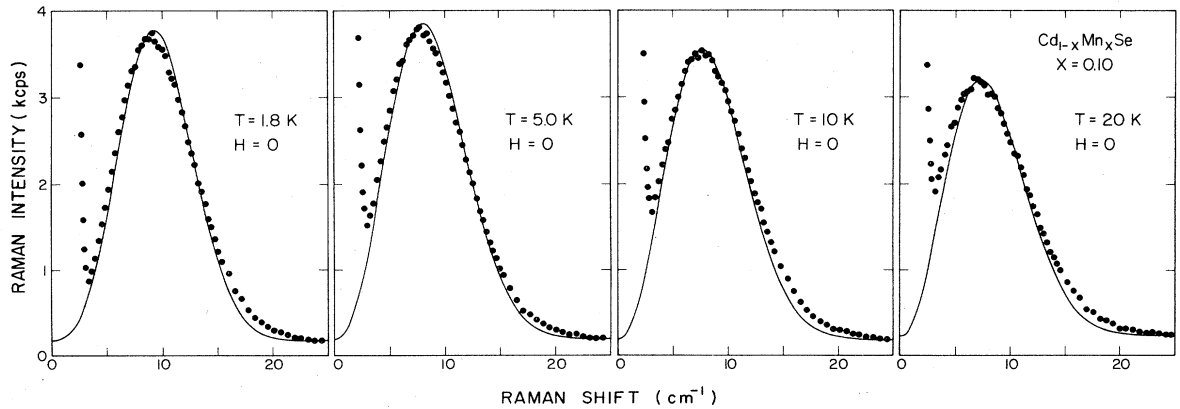


FIG. 22. Zero-field spin-flip Raman spectra for the $Cd_{1-x}Mn_xSe$, $x=0.10$, sample at $T=1.8$, 5, 10, and 20 K. The scans were recorded in the $(\hat{\sigma}_+,\hat{z})$ polarization. The best-fit curves were generated from Eqs. (3.12)—(3.14) using the same value for $\bar{C}$ in Eq. (3.14). The zero-field parameters derived from these fits are $T_{AF}=1.28$ K and $W_0=0.63$ meV.

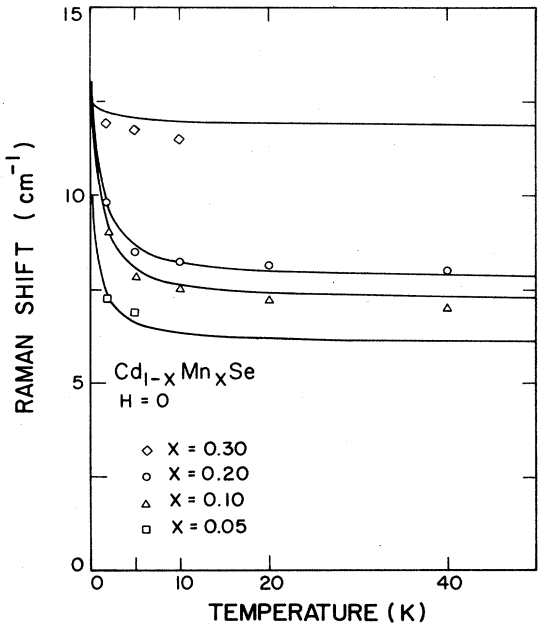


FIG. 23. Temperature dependence of the zero-field spin-flip Raman shift for the $Cd_{1-x}Mn_xSe$, $x=0.05$, 0.10, 0.20, and 0.30, samples. The curves were generated from Eq. (3.22) using the same parameters as for Fig. 21.

we treated $W_0$ and, hence, the effective Bohr radius of the donor orbit, $a$, as an adjustable parameter. These values can be compared with the Bohr radii of the donor orbits for $x=0$,

$$a^*=\hbar^2\kappa/m^*e^2=(0.529\ \text{Å})\kappa m_0/m^* .$$

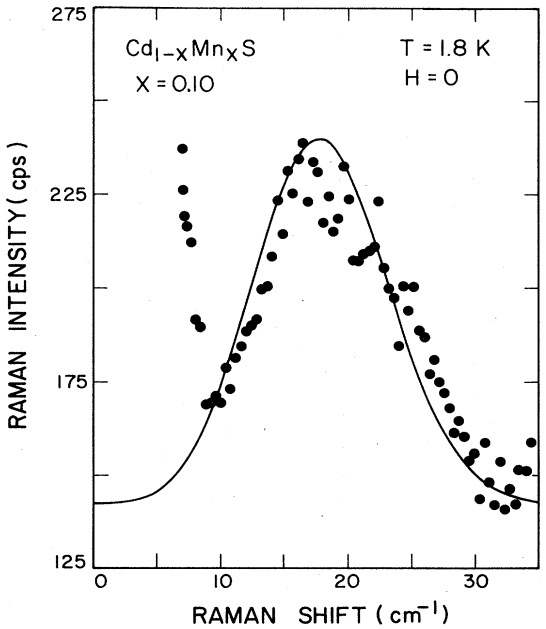


FIG. 24. Zero-field spin-flip Raman spectrum for the $Cd_{1-x}Mn_xS$, $x=0.10$, sample at $T=1.8$ K. The scan was recorded in the $(\hat{\sigma}_+,\hat{z})$ polarization. The best-fit curve was generated from Eqs. (3.12)–(3.14) with $T_{AF}=1.88$ K and $W_0=1.04$ meV.

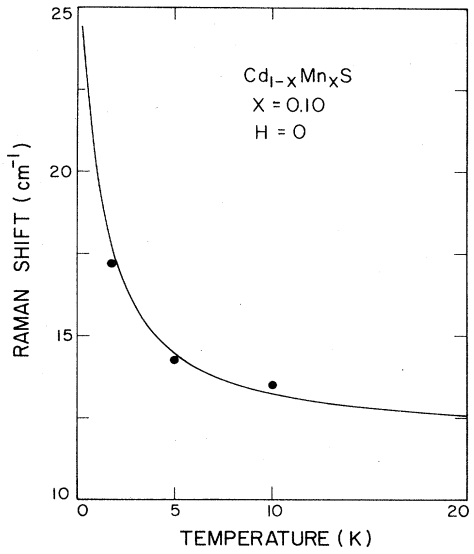


FIG. 25. Temperature dependence of the zero-field spin-flip Raman shift for the $Cd_{1-x}Mn_xS$, $x=0.10$, sample. The curve was generated from Eq. (3.22) with $T_{AF}=1.88$ K and $W_0=1.04$ meV.

These values are 52.4, 43.1, and 23.5 Å for CdTe, CdSe, and CdS, respectively. As described in the theory of Dietl and Spałek,[20] the formation of the bound magnetic polaron causes the orbit of the localized electron to shrink. Using the values of $W_0$ and $\bar{x}$ from Table IV, the values of $a$ in $Cd_{1-x}Mn_xTe$ are 48 Å for $x=0.035$, 40 Å for $x=0.102$, and 28 Å for $x=0.295$. [We assume $N_0=N_0(\text{CdTe})=1.46\times10^{22}$ cm$^{-3}$; the cation density $N_0$ does vary[37] slightly with $x$, but we neglect this here.] The decrease in the orbit size as $x$ is increased is dramatic and is indicative of the contribution that the magnetic interac-

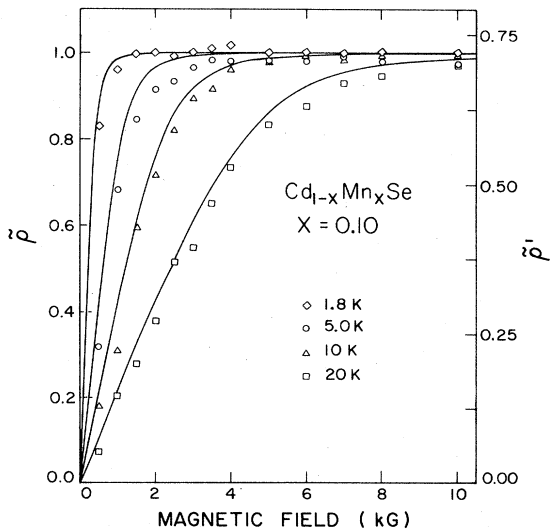


FIG. 26. Magnetic field and temperature dependence of the degree of circular polarization $\tilde{\rho}$ for the $Cd_{1-x}Mn_xSe$, $x=0.10$, sample. The maximum measured value $\tilde{\rho}'=0.72$ is normalized to $\tilde{\rho}=1$. The curves were generated from Eq. (3.27) with $\bar{x}\alpha N_0=10.1$ meV, $T_{AF}=2.20$ K, and $W_0=0.67$ meV.

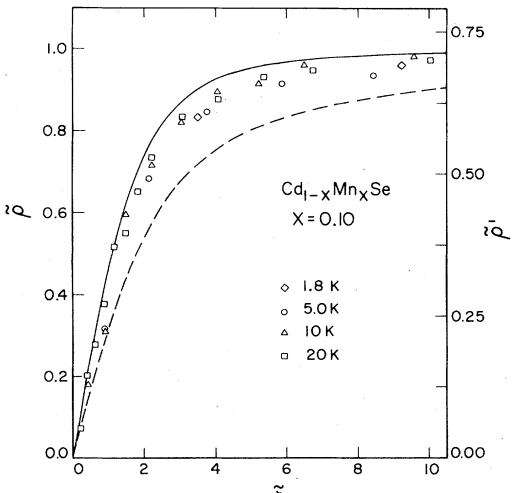


FIG. 27. Dependence of the degree of circular polarization $\tilde{\rho}$ on the parameter $\tilde{\xi}=(\tilde{\Delta}\Delta_0)/4\epsilon_p k_B T$ for the $Cd_{1-x}Mn_xSe$, $x=0.10$, sample. The maximum measured value $\tilde{\rho}'=0.72$ is normalized to $\tilde{\rho}=1$. The solid curve was generated from Eq. (3.27), whereas the dashed curve represents $\rho=\langle\cos\theta\rangle=\coth\xi-1/\xi$ (see Ref. 38).

tion makes to the binding energy of the electron. Using the values of $W_0$ in Table IV and $N_0=N_0(\text{CdSe})=1.78\times10^{22}$ cm$^{-3}$, $a$ is 36 Å for $x=0.051$, 35 Å for $x=0.104$ and 0.129, and 28 Å for $x=0.311$ in $Cd_{1-x}Mn_xSe$. Similarly, the effective Bohr radius is 22 Å for $Cd_{1-x}Mn_xS$ with $x=0.125$ with $N_0(\text{CdS})=2.01\times10^{22}$ cm$^{-3}$. One can thus conclude that the large differences in $W_0$ for different DMS's of comparable $x$ can be primarily attributed to the sizes of the Bohr orbits rather than to variations in $\bar{x}$ and $\alpha N_0$.

### E. Polarization characteristics of spin-flip Raman scattering in DMS's

As mentioned in subsection A, Stokes spin-flip Raman scattering in cubic $Cd_{1-x}Mn_xTe$ is observed in the $(\hat{\sigma}_+,\hat{z})$ and $(\hat{z},\hat{\sigma}_-)$ polarizations for large magnetic fields. For large $H$ with $\mathbf{H}$ being along $\hat{c}||\hat{z}$, Stokes spin-flip scattering is present in the $(\hat{\sigma}_+,\hat{z})$ polarization and absent in the $(\hat{\sigma}_-,\hat{z})$ polarization for the wurtzite $Cd_{1-x}Mn_xSe$ and $Cd_{1-x}Mn_xS$ samples. Our polarization results, as well as those of other studies,[15,16] agree with the selection rules appropriate to electrons bound to donors in crystals with the wurtzite structure as determined by Thomas and Hopfield.[2]

The polarization results discussed above refer to Raman scattering in a large applied magnetic field, which aligns the electron-spin-quantization axes, such that $\Delta||\mathbf{H}$. In the absence of an applied field, the distribution of $\Delta$ is completely isotropic. As the field is turned on, the quantization axes will begin to align themselves in a manner that is dependent on the sample temperature and other parameters, such as composition. This degree of alignment can be determined from polarization studies as a function of magnetic field and temperature.

Here we discuss the results for the $Cd_{1-x}Mn_xSe$, $x=0.10$, sample. With $\mathbf{H}||\hat{c}||\hat{z}$, the Stokes Raman intensities were measured in the $(\hat{\sigma}_+,\hat{z})$ and $(\hat{\sigma}_-,\hat{z})$ polarizations for $H\leq10$ kG and $T=1.8$, 5, 10, and 20 K. It is useful to characterize the intensity of the scattered radiation by a parameter $\rho$ defined as

$$\rho=\frac{I_+-I_-}{I_++I_-}\ , \tag{3.24}$$

where $I_+$ and $I_-$ are the Stokes intensities in the $(\hat{\sigma}_+,\hat{z})$ and $(\hat{\sigma}_-,\hat{z})$ configurations, respectively. As mentioned in subsection D, the result of Eq. (3.14) does not include the angular dependence of the Raman matrix elements. Since the Raman scattering proceeds through intermediate states affected by the applied magnetic field and the resulting magnetization, the angular relationship of $\Delta$ with $\mathbf{H}||\hat{c}$ has a pronounced effect on the Raman cross section. Alov *et al.*[15] propose that, to within a common Boltzmann factor,

$$I_+\propto\left\langle\cos^4\frac{\theta}{2}\right\rangle \text{ and } I_-\propto\left\langle\sin^4\frac{\theta}{2}\right\rangle\ , \tag{3.25}$$

where $\theta$ is the angle between the local quantization axis $\Delta$ and the applied magnetic field. Although this result was derived for a DMS of the wurtzite structure, a similar argument yields the same result for cubic $Cd_{1-x}Mn_xTe$. Using the probability distribution of Dietl and Spałek,[21] the expectation value of a function of $\theta$, $f(\theta)$, will have the following dependence on $\Delta$:

$$\langle f(\theta)\rangle=\int d\Omega\,\Delta^2 f(\theta)P(\Delta)\ , \tag{3.26}$$

where $P(\Delta)$ is given by Eq. (3.10). A straightforward calculation yields a result similar to that of Alov *et al.*,[15] viz.,

$$\rho(\xi)=\frac{\xi(\xi\coth\xi-1)}{\xi^2+1-\xi\coth\xi}\ , \tag{3.27}$$

where $\xi=(\Delta\Delta_0)/(4\epsilon_p k_B T)$. From this result, it is clear that $\rho$ should vary not only with magnetic field and temperature, but also with the magnitude of the spin splitting, resulting in different portions of the rather broad Raman feature exhibiting different degrees of polarization.

The results in Eq. (3.25) were derived by Alov *et al.*,[15] with the assumption that the difference in the energies of the intermediate states associated with the $(\hat{\sigma}_+,\hat{z})$ and $(\hat{\sigma}_-,\hat{z})$ processes is negligible, or, in other words, that the Raman scattering occurs with laser energies much smaller than the energy-band gap. This is not strictly the case, when experiments are performed with laser energies that approach resonance conditions, and the functional form of the angular dependence in Eq. (3.25) could depend on the laser wavelength used in the experiment.

The experimentally determined values of $\rho$ for the peak Raman shift, $\tilde{\rho}'$, are plotted in Fig. 26 as a function of magnetic field and temperature. As can be seen in the figure, the measured values saturate at $\tilde{\rho}'=0.72$. This value lower than unity can be attributed to the limitations inherent to polarization measurements and we assume the saturation value of $\tilde{\rho}'$ to correspond to a complete alignment of the quantization axes $\Delta$ leading to $\tilde{\rho}=\rho(\tilde{\xi})=1$, where $\tilde{\xi}=(\tilde{\Delta}\Delta_0)/(4\epsilon_p k_B T)$. The curves of Fig. 26 were

generated from Eq. (3.27) using the parameters in Table IV. In Fig. 27 we plot $\tilde{\rho}'$ as a function of the dimensionless parameter $\tilde{\xi}$, allowing a comparison of the data for different magnetic fields and temperatures in a convenient manner. The solid line in Fig. 27 represents Eq. (3.27); the experimental results lie just below this line, perhaps reflecting the effects of the near resonance of the laser energy with the band gap. The dashed line in the figure corresponds to

$$\rho = \langle \cos\theta \rangle = \coth\xi - 1/\xi \ ,$$

as proposed by Planel.[38] As can be seen, it gives a poor agreement with the experimental data.

## IV. CONCLUSION

The experimental results presented in this paper represent a comprehensive spin-flip Raman scattering study of electrons bound to donors in the diluted magnetic semiconductors $Cd_{1-x}Mn_xTe$, $Cd_{1-x}Mn_xSe$, and $Cd_{1-x}Mn_xS$ for $x \lesssim 0.30$. The characteristics of Raman scattering associated with the spin-flip transitions of electrons bound to donors are summarized here.

(1) For low Mn concentrations, the Raman shifts exhibit a Brillouin-type magnetic field and temperature dependence characteristic of a paramagnetic system.

(2) As $x$ is increased, a zero-field spin splitting is observed and the effects of the antiferromagnetic coupling are manifested in increasing deviations from Brillouin-type behavior. The Raman shifts can be described using the mean-field approximation with composition-dependent parameters $\bar{x}$ and $T_{AF}$. These parameters exhibit a temperature dependence for $T \geq 40$ K.

(3) The measured Raman shifts were analyzed using the statistical-mechanical theory of Dietl and Spałek. For low compositions, $x \lesssim 0.15$, the theory describes the experimental results very well except for high temperatures ($T \geq 40$ K) or very low magnetic fields, which can be accounted for by allowing the parameters of the theory, $\bar{x}$ and $T_{AF}$, to assume magnetic field and temperature dependences. For $x \gtrsim 0.15$, the theory is not as successful in providing an adequate description of the measured Raman shifts.

(4) The polarization characteristics of the spin-flip Raman feature were compared with a model that includes the angular dependence of the Raman matrix elements.

## ACKNOWLEDGMENTS

The experimental work reported in this paper was supported by a joint Massachusetts Institute of Technology—Purdue University project under U.S. Office of Naval Research Grant No. N00014-81-K-0654. Aid from the Central Laser Facility and the Central Materials Preparation Facility operated under National Science Foundation—Materials Research Laboratories (NSF-MRL) Program No. DMR-80-20249 is acknowledged. One of us (D.L.P.) acknowledges support by the Eastman Kodak Company. We thank Professor J. K. Furdyna for many stimulating discussions, Dr. D. Yoder-Short for performing the invaluable electron-probe microanalysis, and Dr. W. Giriat and Dr. R. R. Galazka for providing some of the samples. The $Cd_{1-x}Mn_xS$ samples were obtained from the Eagle-Pitcher Company.

[1]R. E. Slusher, C. K. N. Patel, and P. A. Fleury, Phys. Rev. Lett. **18**, 77 (1967).
[2]D. G. Thomas and J. J. Hopfield, Phys. Rev. **175**, 1021 (1968).
[3]C. K. N. Patel and E. D. Shaw, Phys. Rev. Lett. **24**, 451 (1970).
[4]A. Mooradian, S. R. J. Brueck, and F. A. Blum, Appl. Phys. Lett. **17**, 481 (1970).
[5]T. W. Walker, C. W. Litton, D. C. Reynolds, T. C. Collins, W. A. Wallace, J. H. Gorrell, and K. C. Jungling, in *Proceedings of the XI International Conference on the Physics of Semiconductors, Warsaw, 1972* (Elsevier, New York, 1972), p. 376.
[6]J. K. Furdyna, J. Appl. Phys. **53**, 7637 (1982).
[7]J. A. Gaj, J. Ginter, and R. R. Galazka, Phys. Status Solidi B **89**, 655 (1978).
[8]A. Twardowski, M. Nawrocki, and J. Ginter, Phys. Status Solidi B **96**, 497 (1979).
[9]J. A. Gaj, R. R. Galazka, and M. Nawrocki, Solid State Commun. **25**, 193 (1978).
[10]F. F. Geyer and H. Y. Fan, IEEE J. Quantum Electron. **QE-16**, 1365 (1980).
[11]M. Nawrocki, R. Planel, G. Fishman, and R. Galazka, in Proceedings of the XV International Conference on the Physics of Semiconductors, Kyoto, 1980, edited by S. Tanaka and Y. Toyazawa [J. Phys. Soc. Jpn. Suppl. A **49**, 823 (1980)]; Phys. Rev. Lett. **46**, 735 (1981).
[12]D. L. Peterson, A. Petrou, M. Dutta, A. K. Ramdas, and S. Rodriguez, Solid State Commun. **43**, 667 (1982).
[13]M. Dobrowolska, H. D. Drew, J. K. Furdyna, T. Ichiguchi, A. Witowski, and P. A. Wolff, Phys. Rev. Lett. **49**, 845 (1982).
[14]D. D. Alov, S. I. Gubarev, V. B. Timofeev, and B. N. Shepel, Pis'ma Zh. Eksp. Teor. Fiz. **34**, 76 (1981) [JETP Lett. **34**, 71 (1981)].
[15]D. L. Alov, S. I. Gubarev, and V. B. Timofeev, Zh. Eksp. Teor. Fiz. **84**, 1806 (1983) [Sov. Phys.—JETP **57**, 1052 (1983)].
[16]D. Heiman, P. A. Wolff, and J. Warnock, Phys. Rev. B **27**, 4848 (1983).
[17]D. Heiman, Y. Shapira, and S. Foner, Solid State Commun. **45**, 899 (1983); **51**, 603 (1984).
[18]K. Douglas, S. Nakashima, and J. F. Scott, Phys. Rev. B **29**, 5602 (1984).
[19]D. Heiman, Y. Shapira, S. Foner, B. Khazai, R. Kershaw, K. Dwight, and A. Wold, Phys. Rev. B **29**, 5634 (1984).
[20]T. Dietl and J. Spałek, Phys. Rev. Lett. **48**, 355 (1982).
[21]T. Dietl and J. Spałek, Phys. Rev. B **28**, 1548 (1983).
[22]For a convenient, comprehensive review, see A. Pajaczkowska, Prog. Cryst. Growth Charact. **1**, 289 (1978).
[23]Y. R. Lee and A. K. Ramdas, Solid State Commun. **51**, 861 (1984).
[24]J. Stankiewicz, Phys. Rev. B **27**, 3631 (1983).
[25]R. R. Galazka, Shoichi Nagata, and P. H. Keesom, Phys. Rev. B **22**, 3344 (1980).
[26]C. D. Amarasekara, R. R. Galazka, Y. Q. Yang, and P. H. Keesom, Phys. Rev. B **27**, 2868 (1983).
[27]Y. Q. Yang, P. H. Keesom, J. K. Furdyna, and W. Giriat, J. Solid State Chem. **49**, 20 (1983).
[28]L. de Seze, J. Phys. C **10**, L353 (1977).

[29]K. Zanio, *Semiconductors and Semimetals, Vol. 13: Cadmium Telluride,* edited by R. K. Willardson and A. C. Beer (Academic, New York, 1978), p. 162.

[30]Details of the experimental setup are given in D. L. Peterson, Ph.D. thesis, Purdue University, 1984 (unpublished).

[31]A. Petrou, D. L. Peterson, S. Venugopalan, R. R. Galazka, A. K. Ramdas, and S. Rodriguez, Phys. Rev. Lett. **48**, 1036 (1982).

[32]A. Petrou, D. L. Peterson, S. Venugopalan, R. R. Galazka, A. K. Ramdas, and S. Rodriguez, Phys. Rev. B **27**, 3471 (1983).

[33]D. L. Peterson, A. K. Ramdas, and S. Rodriguez, in *Proceedings of the 17th International Conference on Physics of Semiconductors, San Francisco, 1984,* edited by J. C. Chadi and W. A. Harrison (Springer, New York, 1985), p. 1401.

[34]S. Venugopalan, A. Petrou, R. R. Galazka, A. K. Ramdas, and S. Rodriguez, Phys. Rev. B **25**, 2681 (1982).

[35]J. A. Gaj, R. Planel, and G. Fishman, Solid State Commun. **29**, 435 (1979).

[26]Y. Shapira, D. Heiman, and S. Foner, Solid State Commun. **44**, 1243 (1982).

[37]J. K. Furdyna, W. Giriat, D. F. Mitchell, and G. I. Sproule, J. Solid State Chem. **46**, 349 (1983).

[38]R. Planel, in *Springer Lecture Notes in Physics,* edited by G. Landwehr (Springer, Berlin, 1983), Vol. 177, p. 441.